Prediction of the transport, deposition, and absorption of multicomponent E-cigarette aerosols in a subject-specific mouth-to-G10 human respiratory system

Ted Sperry [a], Yu Feng [a,*], Jianan Zhao [a], Chen Song [b], Zhiqiang Shi [b]

[a] *School of Chemical Engineering, Oklahoma State University, Stillwater, OK, 74078, USA*
[b] *Spectrum Dynamic Research Corp., Phoenix, AZ, 85016, USA*

ARTICLE INFO

ABSTRACT

Predicting the transport and deposition of e-cigarette aerosols in human respiratory systems is essential to understand how e-liquid compositions, especially different nicotine forms, can influence the absorption of nicotine in the human lung. Using a newly developed computational fluid-particle dynamics (CFPD) method based on the species transport and discrete phase models, this study simulated and compared the transport dynamics of multi-component e-cigarette aerosols in a subject-specific human respiratory system. Specifically, the experimentally calibrated and validated CFPD model can predict the gas-liquid phase change dynamics of water, propylene glycol (PG), vegetable glycerin (VG), and nicotine in the aerosols during their transport through the pulmonary route. Results indicate that acidity levels in e-liquid can affect nicotine evaporation and that higher levels of acidity can reduce evaporation rates and increase the delivery of nicotine vapor to small airways. The study also found that benzoic acid was more effective in reducing nicotine evaporation compared to lactic acid. Furthermore, increasing the PG/VG ratio in the initial e-liquid composition can potentially lead to a reduction in nicotine evaporation rate, and therefore an increase in the amount of nicotine vapor absorbed in small airways beyond generation 10 (G10). Additionally, droplet size dynamics are influenced more by larger mass components such as PG evaporation and water condensation from the humid air, rather than nicotine. However, the impact of initial e-liquid composition on droplet transport and deposition is relatively insignificant compared to its impact on vapor phase transport and absorption. Lastly, increasing the follow-up inhalation flow rate after puffing increases liquid phase deposition and nicotine vapor absorption from the mouth to G10, but does not significantly affect evaporation and condensation. A decrease in droplet size results in an increase in the nicotine evaporation rate and subsequent absorption by the airways from the mouth to G10.

1. Introduction

Electronic cigarettes (ECs) are designed to reduce dependency on traditional tobacco cigarettes by providing a similar means of nicotine delivery to former smokers. These products have gained popularity since their introduction and have undergone technological advancements. To effectively replace conventional cigarettes for smokers, ECs must be able to deliver comparable levels of nicotine to

the human respiratory system. Specifically, it is believed that providing similar nicotine delivery to the human respiratory system will provide similar satisfaction to smokers when using ECs as compared to conventional cigarettes (Johnson, Patten, Ma, De Biasi, & Wesson, 2022). This could aid smokers in reducing conventional cigarette use and ultimately quitting smoking (Hartmann-Boyce et al., 2021).

To improve nicotine delivery and enhance EC user satisfactions, the device technologies continue to advance, with new challenges to the modeling and research on those topics arising due to the wide variability of EC devices and liquids (Glasser et al., 2017; Owotomo & Walley, 2022). Modifications to the devices and e-liquid formulations serve to differentiate them from similar products, which necessitates the use of more complex methods to model the behavior accurately. Some changes to the devices include increasing the power output to the heating coil, allowing users to customize the power setting, as well as changing the chemistry of the e-liquid with the addition of acidic components (Harvanko, Havel, Jacob, & Benowitz, 2020) to help deliver more nicotine to small airways. An example of improving deep-lung nicotine delivery and user satisfaction is the use of protonated nicotine-salt forms in some EC products (Spahn, Stavchansky, & Cui, 2021), based on the observation that modulating acidity can reduce nicotine volatility and improve delivery (Lipowicz & Piadé, 2004). However, current research methods, such as denuders, are not able to fully capture the complexity of human respiratory systems, making it difficult to predict the transport, phase change, and absorption of EC aerosols in the lungs. Therefore, there is still a lack of research on how initial e-liquid compositions, such as nicotine form, acid type, acid level, PG/VG ratio, and droplet diameter, as well as human factors, such as breathing intensity, affect transport, phase change, distribution, deposition, and absorption of EC aerosol in a physiologically realistic human pulmonary environment (Phalen, Hoover, Oldham, Schmid, & Golshahi, 2021). To understand the complex dynamics of ECs in human respiratory systems and address the current knowledge gap, high-resolution data on the transport of EC liquid-vapor mixtures is needed. This includes spatio-temporal distribution of EC components, velocities, pressures, etc. However, current methods such as *in vitro* and *in vivo* studies have limitations in imaging resolution, flexibility, ethics, and research time. It is impossible to cover all possible ranges of e-liquid compositions and breathing conditions using these methods, especially for highly customizable 3rd and 4th generation ECs (Owotomo & Walley, 2022; Stefaniak, Ranpara, Virji, & LeBouf, 2022). Therefore, a reliable, non-invasive, and time-efficient alternative is needed to supplement existing *in vitro* and *in vivo* studies.

As an alternative, *in silico* models have been developed and applied to revolutionize EC exposure-related studies by overcoming deficiencies of the existing *in vitro* and *in vivo* studies mentioned above. These *in silico* models can be divided into two main categories: stochastic models (Pichelstorfer, Hofmann, Winkler-Heil, Yurteri, & McAughey, 2016; Pichelstorfer, Winkler-Heil, Boy, & Hofmann, 2021) and computational fluid dynamics (CFD)-based multiphase flow models (Asgari, Lucci, & Kuczaj, 2021; Feng, Kleinstreuer, Castro, & Rostami, 2016; Feng, Kleinstreuer, & Rostami, 2015; Haghnegahdar, Feng, Chen, & Lin, 2018; Yang, 2018). Stochastic models, such as the Aerosol Dynamics in Confinement (ADiC) model with the Inhalation Deposition Exhalation of Aerosols in the Lungs (IDEAL) model, use procedurally generated cylindrical representations of branching airways to track the random walk of individual droplets and predict deposition on the airway walls. These models are less physiologically realistic but require less computational resource compared to CFD-based models. Other than the stochastic modeling approach, CFD-based Euler-Euler models (Pourhashem, Owen, Castro, & Rostami, 2020) have been used to predict volatile component transport and absorption in the upper respiratory tract. While Euler-Euler models are able to represent small particles (d_d <250 nm) advection-diffusion behaviors accurately with less computational time compared with Euler-Lagrange models (i.e., computational fluid particle dynamics (CFPD) models), they do require extensive calibrations and corrections in some terms of the governing equations to accurately predict inertial impaction of particles with relatively larger diameters. Additionally, Euler-Euler models are not able to explicitly visualize the trajectories of individual multi-component droplets of the present diameter range through the pulmonary route. Another CFD-based model, i.e., the Euler-Lagrange model or CFPD model (Feng et al., 2015; 2016), considers air and vapors as Eulerian phases with a secondary Lagrangian phase representing multicomponent droplets. Phases are coupled by heat and momentum transfer as well as by mass transfer between the liquid and vapor. Compared to stochastic models and Euler-Euler models, CFPD models are able to explicitly predict the transport and phase change for individual droplets, but at the expense of increased computational demands. Explicit prediction of the transport dynamics of each droplet with evaporation/condensation is beneficial to enhance the fundamental understanding of EC aerosol science, since the phase change of species plays a significant role in aerosol size dynamics, as droplets can experience hygroscopic growth due to condensation of water or shrinkage due to evaporation of volatile components.

Although there are many *in silico* studies on EC aersol dynamics, only one focused on nicotine form effect on EC aerosol delivery in human respiratory systems (Pichelstorfer et al., 2016). So far, no CFD effort has been made to investigate nicotine form impact on the nicotine upake in human respiratory systems. Since various forms of EC devices and e-liquids are in use today (Cohen et al., 2022), a CFD modeling framework is needed that can accurately predict deposition patterns due to diameter and composition changes by capturing relevant aerosol properties, especially the nicotine form influence, which have received limited investigation.

Leveraging the existing in-house CFPD model for EC aerosol dynamics simulations (Feng et al., 2015; 2016), this study aims to explicitly simulate multi-component EC aerosol transport, liquid-vapor phase change, and deposition/absorption in a human respiratory system from mouth to generation (G) 10. The CFPD model in this study has been calibrated and validated to predict the liquid-vapor phase changes for various initial e-liquid compositions and conditions to reflect evaporation/condensation behaviors of new-generation protonated nicotine forms. The differences between protonated and unprotonated nicotine forms on the liquid-vapor phase change of EC aerosol species and the resultant nicotine uptake in the mouth-to-G10 geometry have been investigated. The influence of the carrier relative composition of propylene glycol (PG) and Vegetable Glycerin (VG), as well as various droplet diameters and inhalation flow rates, has also been quantitatively studied. This CFPD study aims to provide a reliable physics-based computational modeling framework and quantitative data to assist regulatory science and legislation agencies in gaining a deeper understanding of nicotine transport and absorption associated with design parameters of EC products, which will improve regulatory oversight and

enhance the health and safety of users (Meissner et al., 2022; Yang, 2018), and to aid researchers and scientists in understanding how to modulate design parameters to optimize the delivered nicotine doses with enhanced nicotine satisfaction and minimized overdose risks.

2. Methodology

2.1. Geometry and mesh

As shown in Fig. 1, The subject-specific airway geometry covering from mouth to generation (G) 10 airway employed in this study was reconstructed from computed tomography (CT) scan images of a 47-year-old healthy male volunteer, who was 174 cm in height and 78 kg in weight, and has no history of respiratory diseases (Zhang, Kleinstreuer, & Hyun, 2012). A General Electric (GE) 64-slice CT scanner was used to take images of 500 mm by 500 mm (i.e., 512×512 pixels on the plane) cross-sections with 2.5 mm image slice thickness. The images were taken from the extra-cranial skull base to the abdominal region. To ensure realism in EC vaping scenarios, the subject was instructed to hold a straw with the same geometric dimensions as the EC during the CT scanning process. To avoid unrealistic reversed flow at outlets and the resultant stability issue in simulations, extending cylindrical tubes were added to the lobar outlets. A circular mouth inlet was created with a hydraulic diameter of 8 mm, which represents the typical opening of EC mouth-pieces. The center of the mouth inlet is located at $(x,y,z)=(0,0,0)$, and the normal direction of the inlet is aligned with the positive z-direction.

Unstructured polyhedron-based CFD meshes were generated using Fluent Meshing 2021 R1 (Ansys Inc., Canonsburg, PA). Five near-wall prism layers were generated with refinement to resolve the airflow boundary layers. The final mesh contains 1,706,817 cells, 8,435,426 faces, and 5,456,776 nodes. Details of the three meshes used in the independence test are listed in Table 1. Mesh independence tests were performed using transient simulations with a constant inlet velocity. The wall boundary conditions were set to be no-slip, and outlets were set to be uniform pressure outlets during inhalation. The mouth inlet velocity is 0.4 m/s, representing the standard puffing flow rate $Q_{in} = 55$ ml per 3 s. Mesh topologies were determined by refining the meshes until grid independence of the flow field solutions was achieved. Specifically, comparisons of jet flow velocity profiles at multiple lines at $t = 3$ s were made to find the final mesh. Lines selected are shown in Fig. 2 (a)-(d), which are at cross-sections z = 0.002684 m, 0.01 m, 0.02 m, and 0.03 m, respectively. The comparisons shown in Fig. 2 (a)–(d) indicate that the numerical predictions have negligible variations between Mesh 2 and Mesh 3. Thus, Mesh 2 was selected as the final mesh for this study.

2.2. Governing equations

Using an updated modeling strategy based on the species transport model and multi-component droplet discrete phase model (DPM) compared with the previous version (Feng et al., 2015; 2016), the CFPD model employed in this study can predict the transport, phase change, and deposition/absorption of multi-component EC aerosols in human respiratory systems (see Fig. 3). The governing equations are presented below.
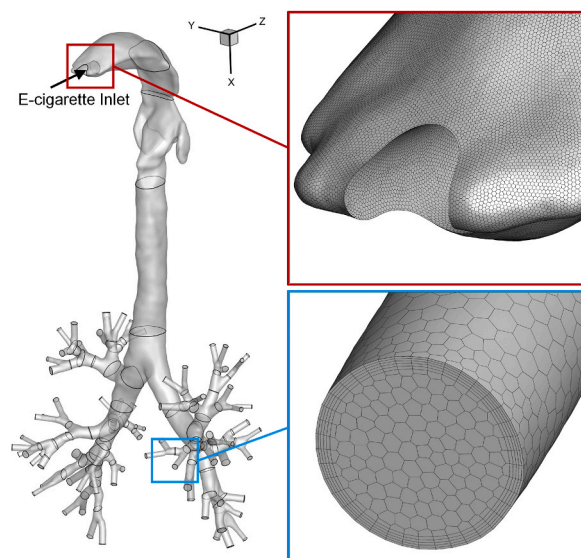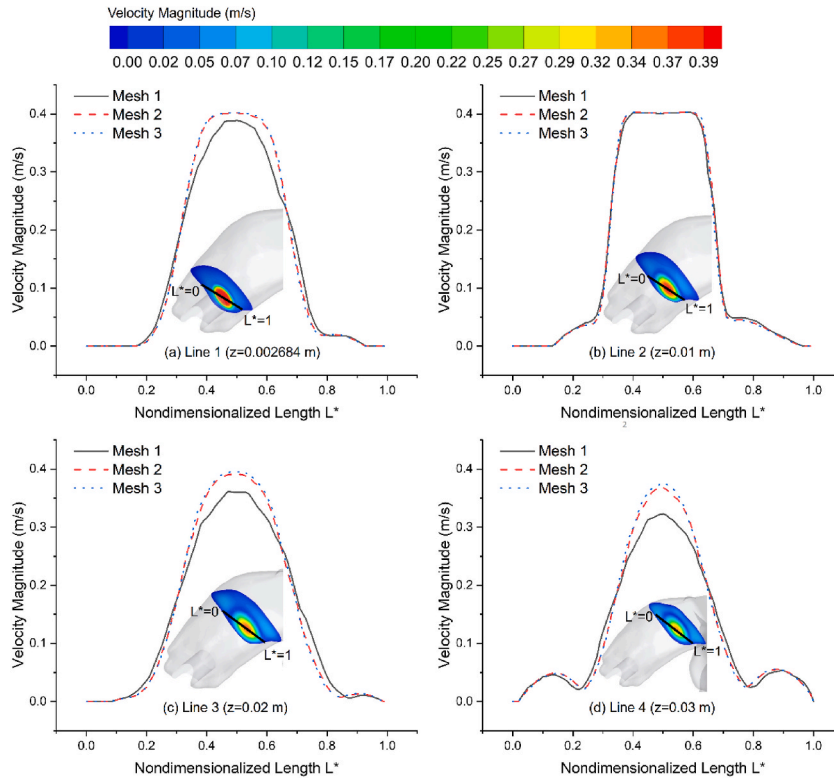

Fig. 1. Geometry and mesh details of the human respiratory system employed in this study.

Table 1

Details of meshes generated for the mesh independence test.

Mesh No.	Cells	Faces	Nodes
1	1,050,144	5,054,877	3,206,317
2	1,706,817	8,435,426	5,456,776
3	3,124,609	16,510,010	11,260,128

Fig. 2. Mesh independence test using the velocity profile comparisons on lines at selected cross-sections: (a) Line 1 at cross-section z = 0.002684 m, (b) Line 2 at cross-section z = 0.01 m, (c) Line 3 at cross-section z = 0.02 m, and (d) Line 4 at cross-section z = 0.03 m.
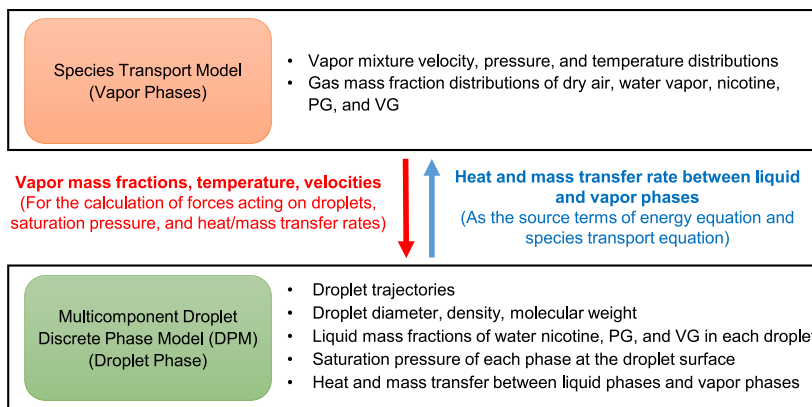
Fig. 3. Modeling framework and data communication of the species transport plus multicomponent droplet DPM model.

2.2.1. Air-vapor mixture (continuous phases)

2.2.1.1. Continuity equation

$$\frac{\partial \rho_{a-v}}{\partial t} + \frac{\partial (\rho_{a-v} u_j)}{\partial x_j} = 0 \tag{1}$$

where ρ_{a-v} is the density of air-vapor mixture, u_j is the velocity tensor.

2.2.1.2. Momentum equation

$$\frac{\partial (\rho_{a-v} u_i)}{\partial t} + \frac{\partial (\rho_{a-v} u_i u_j)}{\partial x_j} = -\frac{\partial p}{\partial x_i} + \frac{\partial \tau_{ij}}{\partial x_j} + \rho_{a-v} g_i \tag{2}$$

where the viscous stress tensor τ_{ij} can be expressed as

$$\tau_{ij} = \mu_{a-v} \left[\left(\frac{\partial u_i}{\partial x_j} + \frac{\partial u_j}{\partial x_i} \right) - \frac{2}{3} \delta_{ij} \frac{\partial u_k}{\partial x_k} \right] \tag{3}$$

Accordingly, the dissipation function Φ in energy equation (see Eq. (5)) can be defined as

$$\Phi = \tau_{ij} \frac{\partial u_i}{\partial x_j} \tag{4}$$

2.2.1.3. Energy equation

$$\frac{\partial (\rho c_p T)_{a-v}}{\partial t} + \frac{\partial (\rho c_p u_j T)_{a-v}}{\partial x_j} =$$

$$\frac{\partial}{\partial x_j} \left[\left(k_{a-v} + \frac{\rho_{a-v} c_{p,a-v} \nu_T}{\mathrm{Pr}_T} \right) \frac{\partial T_{a-v}}{\partial x_j} \right] + \Phi + \frac{\partial}{\partial x_j} \left[\sum_{s=1}^{4} h_s \rho_{a-v} \left(\widetilde{D}_{a-v,s} + \frac{\nu_T}{Sc_T} \right) \frac{\partial Y_{s,v}}{\partial x_j} \right] + S_{v-d}^{(E)} \tag{5}$$

where $c_{p,a-v}$ and T_{a-v} is the specific heat and temperature of air-vapor mixture, respectively. h_s is the convective heat transfer coefficient of the sth species ($s = 1, 2, 3$ and 4), $Sc_T = 0.9$ is the turbulence Schmidt number, ν_T is the turbulent viscosity, and $\widetilde{D}_{a-v,s}$ is the molecular diffusivity of the sth vapor species in the air-vapor mixture. In Eq. (5), the energy source term $S_{v-d}^{(E)}$ is the latent heat of evaporation or condensation which is released or absorbed by the droplets per local mesh cell, i.e.,

$$S_{v-d}^{(E)} = \sum_{s=1}^{4} S_{v-d,s}^{(E)} = \left\{ \sum_{i=1}^{N_{d,cell}} \left[\left(\sum_{s=1}^{4} L_s \bar{j}_s \right) A_d \right]_i \right\} / V_{cell} \tag{6 a and b}$$

where $N_{d,cell}$ is the total droplet number in a specified mesh cell, and V_{cell} is the mesh cell volume. Subscript s denotes the sth species. The governing equation for advection and diffusion of the sth vapor species are expressed as:

$$\frac{\partial (\rho_{a-v} Y_{s,v})}{\partial t} + \frac{\partial}{\partial x_j} \left(\rho_{a-v} u_j Y_{s,v} \right) = \frac{\partial}{\partial x_j} \left[\rho_{a-v} \left(\widetilde{D}_{a-v,s} + \frac{\nu_T}{Sc_T} \right) \frac{\partial Y_{s,v}}{\partial x_j} \right] + S_{v-d,s}^{(Y)} \tag{7}$$

The local vaporized/condensed vapor-mass flow rate of the aerosol components are added to its advection-diffusion equation as a source term $S_{v-d,s}^{(Y)}$ (kg m^{-3} s^{-1}), i.e.,

$$S_{v-d,s}^{(Y)} = \int_{t_{i,start}}^{t_{i,start} + \Delta t_f} \left(\sum_{i=1}^{N_{d,cell}} (\bar{j}_s A_d)_i \right) dt_d / \left(V_{cell} \Delta t_f \right) \tag{8}$$

where $\bar{j}_s$ is the average evaporation/condensation mass flux normal to the droplet surface of the sth component (i.e., $\bar{j}_s > 0$ for evaporation and $\bar{j}_s < 0$ for condensation); and A_d is the droplet surface area. Also, dt_d represents the droplet phase time differential and Δt_f is the flow time step.

2.2.2. Multicomponent droplet transport and size change dynamics (discrete phase)

The Lagrangian approach is chosen to track multi-component droplets, neglecting rotational motion. The governing equations for discrete droplets are the translational equation of droplets as well as the mass and energy conservation laws for droplets.

2.2.2.1. Translational equation of droplets. For predicting EC droplet trajectories, Newton's 2nd law was employed, which can be expressed as (Feng et al., 2018)

$$\frac{d}{dt}\left(m_d u_{d,i}\right) = F_i^D + F_i^L + F_i^{BM} + F_i^G \tag{9}$$

where F_i^D, F_i^L, F_i^{BM}, and F_i^G are the drag force, lift force, Brownian motion-induced force, and gravity, respectively.

2.2.2.2. Mass conservation of droplets. Droplet mass changes due to condensation/evaporation can be calculated by

$$\frac{dm_d}{dt} = -\sum_{s=1}^{m} \int_{surf} j_s dA \approx -\sum_{s=1}^{m} \left(\bar{j}_s \cdot A_d\right) \tag{10a and b}$$

where the average mass flux $\bar{j}_s$ is given by (Turns, 1996)

$$\bar{j}_s = CF \cdot \rho_{a-v} \cdot C_m \cdot Sh \cdot \tilde{D}_{a-v,s} \cdot d_d^{-1} \ln\left[\left(1 - Y_{s,v,cell}\right) / \left(1 - Y_{s,vsurf}\right)\right] \tag{11}$$

Here, Sh is the Sherwood number (Haghnegahdar, Zhao, & Feng, 2019), while $Y_{s,vsurf}$ and $Y_{s,v,cell}$ are the mass fractions of the sth vapor phase at the droplet surface and at the center of the cell where the droplet currently resides, which represents the ambient vapor mass fraction surrouding the droplet. The calibration factor $CF = 0.005$ is introduced to calibrate the difference in the evaporation/condensation rate between the virtual EC aerosol injected and the real EC aerosol due to the difference in their concentrations based on experimental measurements on nicotine vapor retention in denuders. More details can be found in Section 3.1.2. The correction factor C_m for submicron droplets, considering non-continuum effects can be expressed as

$$C_m = \frac{1 + Kn}{1 + \left(\frac{4}{3\alpha_m} + 0.377\right)Kn + \frac{4}{3\alpha_m}Kn^2} \tag{12}$$

where Kn is the Knudsen number, $Kn = 2\lambda_{a-v}/d_d$, in which λ_{a-v} is the mean free path of the air-vapor mixture surrounding the droplet, and $\alpha_m = 1$ is the mass accommodation coefficient (Hinds & Zhu, 2022). Equation (11) is based on the assumption that the distance between the droplet mass center and the mesh cell center is much larger than the droplet radius. Specifically, $Y_{s,v,cell}$ is determined by the advection-diffusion equation (see Eq. (7)), while $Y_{s,vsurf}$ can be calculated by

$$Y_{s,vsurf} = \frac{\rho_{s,vsurf}}{\rho_{a-v}} = \frac{\left(P_{s,vsurf}/\Re_s T_d\right)}{\rho_{a-v}} = \frac{\gamma_s \cdot K_s \cdot X_{s,d} \cdot P_{s,vsat}(T_d)}{\rho_{a-v}(\Re/M_s)T_d} \tag{13a b, and c}$$

Here, $\rho_{s,vsurf}$ is the equivalent density of vapor species s in the air-vapor mixture at the droplet surface; γ_s is the activity coefficient of species s, which is a correction of the evaporation/condensation characteristics of a specific liquid component due to the molecular bonding changes in the pure droplets and in the multi-component droplets (Tu & Ray, 2005); $X_{s,d}$ is the mole fraction of the sth component in the droplet; $\Re_s$ is the species gas constant; T_d is the droplet temperature; and $P_{s,vsat}$ is the temperature-dependent saturation pressure of the pure sth species. Clearly, parameters γ_s and $X_{s,d}$ serve as corrections to the vapor pressure at the surface of multi-component droplets (Raoult's law), while K_s is the correction factor for the Kelvin effect (Hinds & Zhu, 2022), which can be given as

$$K_s = \exp\left[\frac{4\sigma_s M_s}{(\Re\rho_s d_d T_d)}\right] \tag{14}$$

where σ_s is the surface tension of component s at the droplet surface.

2.2.2.3. Energy conservation of droplets

$$m_d c_{p,d}(dT_d / dt) = C_T(k_{a-v} \cdot Nu / d_d)\left(T_{a-v,cell} - T_d\right)A_d - \left(\sum_{s=1}^{N} L_s \bar{j}_s\right)A_d \tag{15}$$

where L_s is the latent heat of the liquid-vapor phase transition of the sth species (L_s is always larger than zero). Also, C_T is the correction factor for submicron droplets (Zhang, Kim, & Kleinstreuer, 2006)

$$C_T = \frac{1 + Kn}{1 + \left(\frac{4}{3\alpha_T} + 0.377\right)Kn + \frac{4}{3\alpha_T}Kn^2} \tag{16}$$

where $\alpha_T = 1$ is the thermal accommodation coefficient (Hinds & Zhu, 2022).

2.3. Material properties

To set up the numerical model correctly, we obtained material properties from open literature and an online database for water, nicotine, PG, and VG (Asgharian, Rostami, Price, & Pithawalla, 2018; Duell, 2019; Fisenko et al., 2021; John et al., 2018; Li & Hopke,

1993; Siitsman, Kamenev, & Oja, 2014; Zhang et al., 2012). Material properties are listed in Table 2. Specifically, the generalized Antoine equation for nicotine saturation pressure $p_{sat,nicotine}$ in Pa as a function of temperature T in K used in this study can be given as (Siitsman et al., 2014)

$$\log_{10} \frac{p_{sat,nicotine}}{\chi_s \gamma_s 10^3} = \left[6.158 - \frac{1827.4}{T - 80.977} \right] \tag{17}$$

where χ_s is the nicotine mole fraction and γ_s is the activity coefficient that was calibrated based on the headspace vapor pressure data of nicotine in multiple e-liquid samples with different PG/VG ratio, and acid/nicotine ratio. Expressions of γ_s as a function of nicotine forms, PG/VG ratio, and acid/nicotine ratio can be found in Section 3.1.1.

VG's evaporation is modeled but negligble due to its much lower volatility than nicotine, PG, and water. Specifically, using the Antoine equation (Richardson, 1886; Stull, 1947) to estimate the VG and PG saturation pressure in Pa, i.e.,

$$\log_{10} \frac{p_{sat,VG}}{10^5} = 3.93737 - 1411.531 / (T - 200.566) \ (456.4 \ \text{K} < T < 533.6 \ \text{K}) \tag{18}$$

$$\log_{10} \frac{p_{sat,PG}}{10^5} = 6.07936 - 2692.187 / (T - 17.94) \ (318.7 \ \text{K} < T < 461.4 \ \text{K}) \tag{19}$$

It is worth mentioning that $p_{sat,VG}$ much less than $p_{sat,PG}$ with 2 order of magnitude difference. Therefore, VG behaves highly non-vaporable compared with PG, water, and nicotine in the CFPD simulations.

Water saturation pressure in Pa was defined as a function of temperature T in K, i.e.,

$$\log_{10} \frac{760 p_{sat,water}}{101325} = 8.07131 - 1730.63 / (233.426 + T - 273.15) \tag{20}$$

2.4. Initial and boundary conditions

2.4.1. Initial EC droplet composition and size

The initial droplet compositions (i.e., e-liquid compositions) investigated in this study include 3 variables, i.e., (1) nicotine type and acid type (benzoic acid or lactic acid), (2) initial acid/nicotine ratio, and (3) initial PG/VG ratio. Specifically, based on the compositions of available commercial EC products in the market (Shamout et al., 2021), the initial droplet compositions investigated in this study are listed in Table 3 associated with case numbers. The cases compared are meant to represent a range of previous and current generations of EC technologies and allow comparisons to inform future studies and the development of EC devices. Monodispersed droplet suspensions were assumed. Three initial droplet diameters ($d_{d,ini} = 500$, 800, and 1000 nm) were employed to investigate how initial droplet size can influence nicotine evaporation/condensation and absorption in human respiratory systems. Droplet diameter ranges were determined based on experimental measurements (Sundahl, Berg, & Svensson, 2017).

2.4.2. Initial liquid-vapor partitions in EC aerosols

The liquid-vapor partitions for volatile components in EC aerosols at the mouth inlet were set as ratios of vapor mass to liquid mass for each species. The only vapor phase components at the inlet are water and nicotine during the inhalation of aerosol droplets, followed by humid air without nicotine for the remaining 3 s of inhalation. Per the recommendation from experimentalists, no PG or VG vapors were assumed at the mouth inlet, and the nicotine vapor phase is 0.58% of liquid nicotine mass in initial EC aerosols. The water vapor mass fraction was calculated based on the condition that the relative humidity (RH) of the inhaled air-EC aerosol mixture

Table 2
Material properties of species in EC aerosols.

Property	Nicotine	PG	VG	Water	References
Density [kg/m^3]	1010	1036	1261	1000	Asgharian et al. (2018)
Molecular Weight [g/mol]	162.23	76.09	92.09	18.02	https://pubchem.ncbi.nlm.nih.gov/
Surface Tension [N/m]	38.61e-3	36.0e-3	64.0e-3	73.1e-3	Asgharian et al. (2018)
Latent Heat [J/kg]	450	914	974	2250	Asgharian et al. (2018)
Thermal Conductivity [W/mK]	0.1510	0.1470	0.2860	0.6000	Asgharian et al. (2018)
Boiling Point at 1 atm [K]	520.15	461.15	563.15	373.15	https://pubchem.ncbi.nlm.nih.gov/
Binary Diffusivity in Air [m^2/s] (Temperature T in K)	$0.65e-5 \times (T/298)^{1.75}$	1.24e-05	1.12e-05	$1.95e-5 \times (T/298)^{1.5}$	(Asgharian et al., 2018; John et al., 2018)
Specific Heat [J/kgK]	1757	2500	2370	4181	Asgharian et al. (2018)
Saturation Vapor Pressure [Pa]	Eqs. (17)-(20)				(Duell, 2019; Fisenko et al., 2021; Richardson, 1886; Stull, 1947)
Activity Coefficient	Eqs. (21)-(23)	γ_{PG}[a]	1.0	γ_w[a]	(Kiraz, Karadağ, & Muradoğlu, 2008; Tu & Ray, 2005)

[a] $\gamma_w = \dfrac{c_1}{\left[1 + \dfrac{c_1}{c_2} \dfrac{\chi_w}{1 - \chi_w} \right]}$ and $\gamma_{PG} = \dfrac{c_2}{c_1} (2\sqrt{c_1 \ln \gamma_w} + \ln \gamma_w + c_1)$, where $c_1 = -0.3049$ and $c_2 = -0.8551$.

Table 3
Case numbers with the associated initial compositions in mass fraction for EC droplets.

Case	Nicotine	Acid Type	Acid/Nicotine Ratio	PG	VG	PG/VG Ratio
Freebase	3%	None	0	47.5%	47.5%	1:1
1B	3%	Benzoic	1:3	47.5%	47.5%	1:1
2B	3%	Benzoic	1:1	47.5%	47.5%	1:1
1L	3%	Lactic	1:3	47.5%	47.5%	1:1
2L	3%	Lactic	1:1	47.5%	47.5%	1:1
2575	3%	None	0	24.25%	72.25%	1:3
7525	3%	None	0	72.25%	24.25%	3:1
2575B	3%	Benzoic	1:1	24.25%	72.25%	1:3
7525B	3%	Benzoic	1:1	72.25%	24.25%	3:1

is RH = 50%. The initial temperature of the air-EC aerosol is 300 K (Sleiman et al., 2016).

2.4.3. Mouth inlet conditions

Using a standard flow rate to represent puffing (i.e., 55 ml per 3 s which is equal to 18.3 ml/s), humid air and EC aerosol will be inhaled through the mouth inlet, followed by a step up to an inhalation flow rate of humid air entering the mouth inlet of 500 ml/s (Q_{follow} = 30 L/min) for most cases or 1000 ml/s (Q_{follow} = 60 L/min) for the case shown in Section 4.7 with no additional EC aerosols for another 3 s. Therefore, only the puffing and the follow-up inhalation phase were simulated in this study. No breath hold or exhalation was simulated. As mentioned in Section 2.4.2, The mouth inlet conditions of the simulations represent a room at 300K, with RH = 50%, which represents 1.09% water vapor in the air by weight. Specifically, the total liquid nicotine mass inhaled is 2.4 ng over the puffing period, and the total vapor nicotine mass inhaled is 0.58% of the total liquid nicotine mass inhaled. All cases shown use identical boundary values for ease of comparison. No PG or VG vapors were inhaled during the puffing period. For the remaining time during simulations with the after-puffing inhalation, the mass fractions of all vapor phases other than water are zero. The total number of droplets continuously inhaled from the mouth inlet is 1,688,000.

2.4.4. Airway wall boundary conditions

The boundary conditions of the airway walls were set to reflect the physiologically realistic conditions of human pulmonary routes. Airways were assumed to be static, and the non-slip velocity boundary condition was assigned at the airway walls. Wall temperatures are 310.15 K, which is body temperature. Since these walls are lined with mucus in the human body, RH is set to 100%, which represents a water vapor mass fraction of 3.87%. Fast absorption of nicotine is assumed at the airway wall. Therefore, the Dirichlet boundary condition is assigned (i.e., $Y_{nicotine,v}|_{wall}$ = 0). For droplet deposition, a 100% trapped wall was applied at the airway walls due to the presence of mucus. Specifically, when the distance between the geometric center of the droplet and the airway wall is less than or equal to the droplet diameter, it is considered trapped and absorbed.

2.4.5. Small airway outlet conditions

Zero-gauge pressures were applied at all outlets. For droplet transport, an "escape" boundary condition was applied at all outlets. For vapor transport, a zero-gradient of vapor concentration was applied at all outlets.

2.5. Numerical setup

Ansys Fluent 2021 R1 (Ansys Inc., Canonsburg, PA) was used to run the multi-component EC aerosol transport simulations using the CFPD model. The governing equations were discretized using the finite volume method and 2nd-order schemes in both time and space. To ensure numerical stability, the flow time step employed was 0.001 s. The droplet time step ranges from 1.0e-4 to 1.0e-3 s. Convergence was considered achieved when all residuals became lower than 1.0e-4. Numerical simulations were performed on a local Dell Precision T7810 workstation (Intel® Xeon® Processor E5-2643 v4 with dual processors, 24 cores and 128 GB RAM) and a local Dell Precision T7910 workstation (Intel®Xeon® Processor E5-2683 v4 with dual processors, 64 cores, and 256 GB RAM). In-house user-defined functions (UDFs) were developed and used to customize the CFPD solver, and achieved the following functions, i.e.,

(1) Define saturation pressures vs. temperature for water, PG, VG, nicotine,
(2) Calculate and return the droplet surface saturated vapor pressure, which considers the Kelvin effect, Rault's law, and the deviation from the ideal solution behavior of the multi-component liquid mixture using activity coefficients.
(3) Define heat and mass balance source terms for species in droplets and vapors,
(4) Define the DPM time step,
(5) Update the density of the droplet at each droplet time step based on the updated mass fractions of multi-component in the droplet, and
(6) Extract and store EC droplet and vapor deposition/absorption data.

3. Model validation and calibrations

3.1. Model calibrations

3.1.1. Nicotine activity coefficient (γ_s)

To accurately capture how the initial composition of e-liquid can affect the evaporation/condensation behaviors of nicotine liquid, the activity coefficient γ_s has been calibrated as a function of PG/VG ratio and acid/nicotine ratio, by the comparisons of "effective" saturation pressures vs. experimental data. For nicotine with different PG/VG ratios, acid types and levels, calibrations can be found in Fig. 4 (a), (b) and (c). Specifically, for nicotine salt with lactic acid, γ_s can be given as

$$\gamma_s = C_{acid}\left(-0.3619\alpha^2 - 0.1517\alpha + 0.8004\right) \tag{21}$$

$$C_{acid} = 2.371 \exp(-1.812\beta) \tag{22}$$

where $\alpha = \frac{PG}{PG+VG} \in [0, 1]$ and $\beta = \frac{Acid}{Nicotine} \in [0.2, 3]$. α and β are both mass ratios.

For nicotine salt with benzoic acid, γ_s can be defined by Eq. (21), but with a different correction factor C_{acid}, i.e.,

$$C_{acid} = 1.541 \exp(-1.846\beta) \tag{23}$$

where $\beta \in [0.2, 3]$. It is worth mentioning that e-liquid with $\beta = 0$ is for freebase nicotine, where $C_{acid} = 1.0$. For nicotine with lactic acid, $R^2 = 0.9302$ for the activity coefficient calculated by Eqs. (21) and (22). For nicotine with benzoic acid, $R^2 = 0.9792$ for the activity coefficient calculated by Eqs. (21) and (23).

3.1.2. Calibration factor (CF)

The calibration factor *CF* in Eq. (11) was introduced to revise the evaporation/condensation rate due to the differences in EC aerosol droplet number concentration used in the CFPD simulation and in real EC aerosols. It is worth mentioning that reducing the EC aerosol concentration on droplet number density flow rate, is to enhance the balance between computational efficiency in the CFPD simulations. Specifically, in real e-cigarette aerosols, droplet number density is estimated to be approximately $2.5 \times 10^7 \pm 7 \times 10^6$ droplets/puff (Li, Lee, Nguyen, & Zhu, 2020). With the reduced droplet number density in the simulations compared with real EC aerosols, the species evaporation rate could be overestimated. Therefore, to ensure the correct evaporation rate can be captured, *CF* was introduced to modify the condensation/evaporation rate magnitude. Specifically, *CF* was determined by comparing the nicotine penetration percentages between numerical simulation results using the CFPD model and experiments through the same denuder using the EC aerosols with their original concentration. Specifically, *CF* applies to all components simultaneously, while the individual evaporation of those components depends on the vapor pressure of individual components. $CF = 0.005$ can provide good agreement on nicotine penetration compared with experiments. Details of the calibration can be found in **Appendix A**.

3.2. Model validations

To guarantee the reliability of the CFPD model developed in this study, the key is to evaluate the accuracy of evaporation/condensation predictions of different species, including water, PG, VG, and nicotine. The CFPD model on vapor absorption and particle transport and deposition predictions in our previous publications (David, Parmentier, Taurino, & Signorell, 2020; Li & Hopke, 1993;
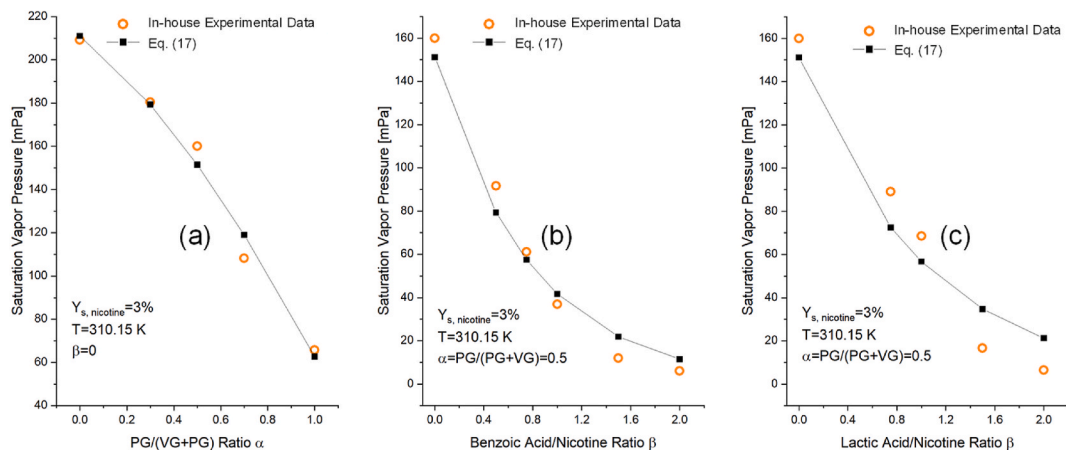

Fig. 4. Comparisons of headspace vapor pressures of nicotine between the predictions using Eqs. (21)-(23) and the experimental data for (a) Freebase nicotine with different PG/(VG + PG) ratios, (b) Nicotine with different benzoic acid/nicotine ratios, and (b) Nicotine with different lactic acid/nicotine ratios.

Smolík, Džumbová, Schwarz, & Kulmala, 2001; Tu & Ray, 2005; Zhang et al., 2006; Zhang et al., 2012). Therefore, only the new validations on evaporation/condensation predictions are presented in this section. Specifically, multi-component EC droplet size change dynamics were simulated and compared with experimental data (i.e., time variations of a single EC droplet composition time profiles) quantified using counter-propagating optical tweezers (CPT) with single-droplet Raman scattering measurement (David et al., 2020). Specifically, the droplet initial composition is 2% nicotine, 30% VG, and 68% PG with pH = 9.9. The initial droplet diameter $d_{d,ini}$ is 6 μm. The ambient temperature is 293.15 K and RH is 65%. Fig. 5 (a)-(d) compare the mass fraction changes of water, nicotine, PG, and VG up to 180 s between the CFPD simulation results and experimental measurements. Good agreement can be found not only for the composition temporal variations. It is worth mentioning that due to the relatively faster PG evaporation in the first 5 s, nicotine mass fraction increases accordingly because of the total mass loss of the droplet (see Fig. 5 (b)). With continuous nicotine evaporation and reduced evaporation rate of PG, the mass fraction of nicotine decreases after approximately 5 s. The good agreement shown in Fig. 5 (a)–(e) demonstrates the capability of the CFPD model to predict the evaporation and condensation of multiple species in EC aerosols. Additional validations on droplet size change dynamics can be found in previous publications (Feng et al., 2015; 2016; Haghnegahdar et al., 2019).

4. Results and discussion

4.1. Aerosol velocity and RH distributions at the sagittal plane

Characteristics of pulmonary airflow velocity field and RH distribution are significant factors that can influence inhaled EC aerosol transport, phase change, deposition, and absorption in human respiratory systems. Therefore, to unveil the key features of the pulmonary flow field data during the puffing and follow-up inhalation, the unsteady pulmonary airflow velocity fields at the sagittal plane of the respiratory system for two representative cases are visualized in Figs. 6 and 7, i.e., Case Freebase with Q_{follow} = 30 L/min and Case 2B with Q_{follow} = 60 L/min. It can be found that during the puff, the mouth jet was gradually formed and extended to the pharynx from t = 0.1 s–0.5 s in both cases. Differences in the jet intensity and secondary flow exist during the follow-up inhalation between the two cases due to the different inhalation flow rate. Specifically, with Q_{follow} = 60 L/min, Fig. 7 (g) and (h) show the mouth jet has a
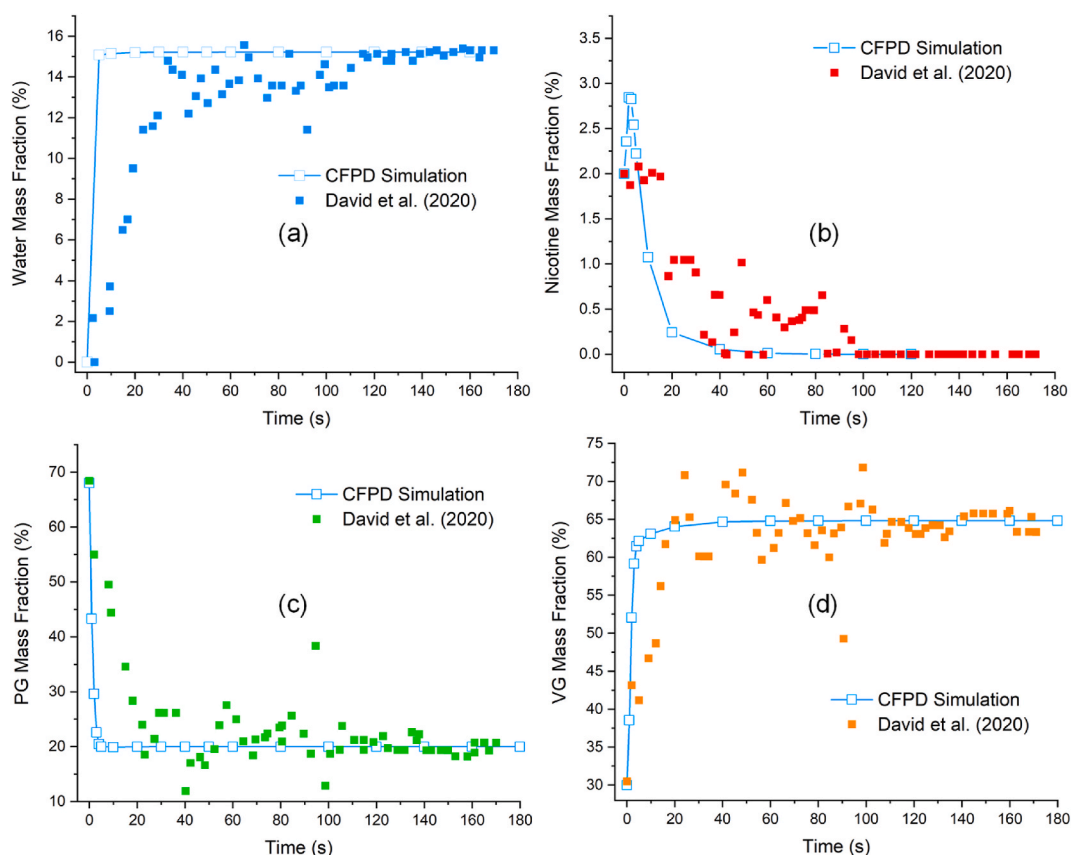

Fig. 5. Comparisons between the numerical predictions and experimental data (David et al., 2020) on the time evolutions of the droplet composition change in an EC droplet: (a) Water mass fraction vs. time, (b) Nicotine mass fraction vs. time, (c) PG mass fraction vs. time, and (d) VG mass fraction vs. time.
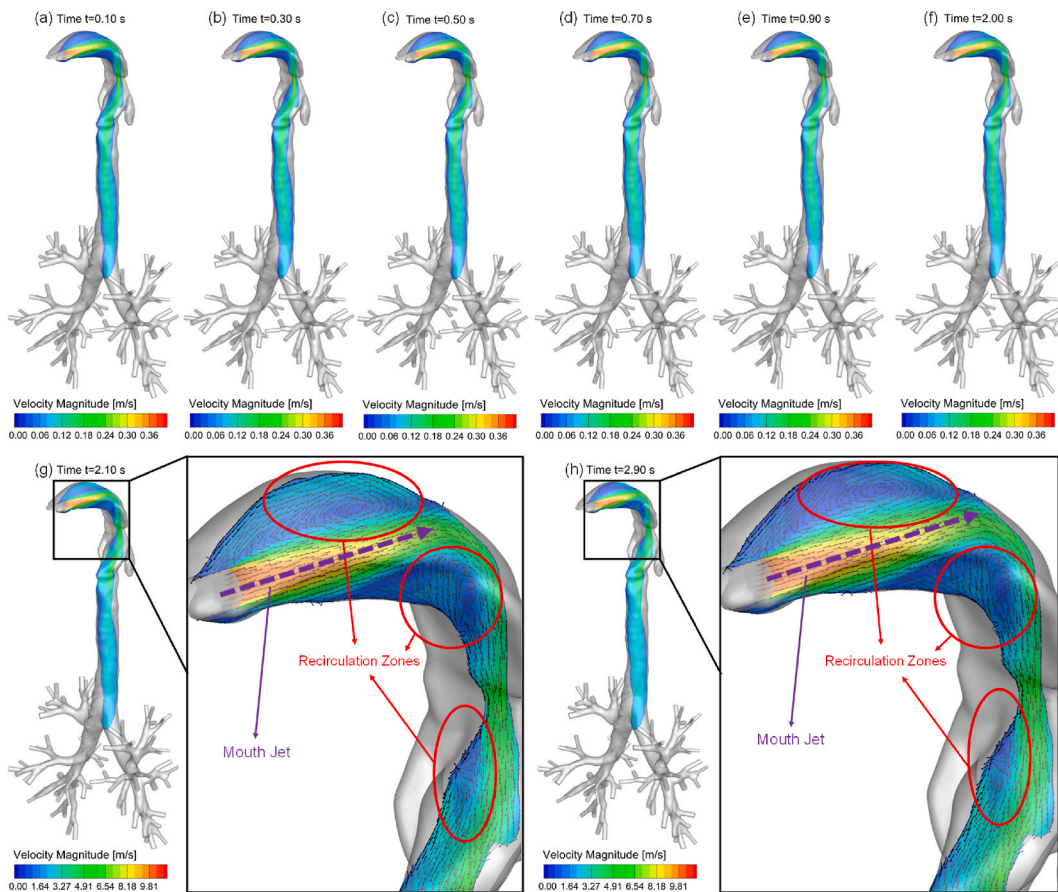
Fig. 6. Evolvement of the airflow velocity magnitude contour and vector field at the sagittal plane of the human respiratory system of the freebase nicotine case with 18.3 ml/s during puffing and a follow-up inhalation flow rate equal to 30 L/min for remaining duration: (a) t = 0.10 s, (b) t = 0.30 s, (c) t = 0.50 s, (d) t = 0.70 s, (e) t = 0.90 s, (f) t = 2.00 s, (g) t = 2.10 s, and (h) t = 2.90 s.

higher velocity compared with Fig. 6 (g) and (h). With the high-velocity jet core, recirculation zones were formed near the upper palate, front pharynx, and front larynx (see the red circles in Fig. 6 (g), 6 (h), 7 (g), and 7 (h). Q_{follow} does not influence the locations of those recirculation zones significantly. The mouth jet, impingement at the pharynx, and the recirculation flows in the upper airway indicate the unevenness of the inertial impaction, interception, and dispersion effects on EC droplet deposition in the upper airway, which will be discussed in Section 4.3.

Since water vapor mass fraction distributions influence the droplet size change dynamics during their transport, Figs. 8 and 9 compare the water vapor distributions in human respiratory systems using volume rendering at multiple time stations for Case Freebase with Q_{follow} = 30 L/min and Case 2B with Q_{follow} = 60 L/min. Specifically, a high water vapor mass fraction means high RH. It can be observed that during the puff (see Fig. 8 (a)–(f) and Fig. 9 (a)–(f)), the inhaled EC aerosols with low RH = 50% dominantly altered the water vapor distributions from the mouth to larynx. It can also be observed that airway walls are always saturated with RH = 100%. Therefore, with the relatively much lower flow rate during the puff compared with the follow-up inhalation, the low RH concentration can only be observed before the inhaled air-aerosol mixture reaches the glottis because of the limited convection effect compared with the diffusion effect. The water vapor is almost saturated from the glottis to airway outlets during the puff. In contrast, Fig. 8 (g)–(l) and Fig. 9 (g)–(l) demonstrate that with the much higher inhalation flow rates, the RH from the mouth to G10 is much lower during the follow-up inhalation period compared with the puff period. Furthermore, it can be observed from Fig. 9 (g)–(l) that with more dominant convection effect, the tracheobronchial (TB) tree in Case 2B with Q_{follow} = 60 L/min has lower RH compared with Case Freebase with Q_{follow} = 30 L/min shown in Fig. 8 (g)–(l). It is worth mentioning that although Case Freebase with Q_{follow} = 30 L/min and Case 2B with Q_{follow} = 60 L/min has different nicotine forms, Section 4.4 proves that the nicotine form has negligible influence on the liquid-vapor phase change of water (see Fig. 13 (b)). Therefore, the difference of RH distributions in Fig. 8 (g)–(l) and Fig. 9 (g)–(l) is due to the difference in convection effect induced by Q_{follow}. It can also be observed from Figs. 8 and 9 that the recirculation zones shown in Figs. 6 and 7 always have relatively higher RH compared with the neighboring regions, which is also due to the less dominant convection effect locally.
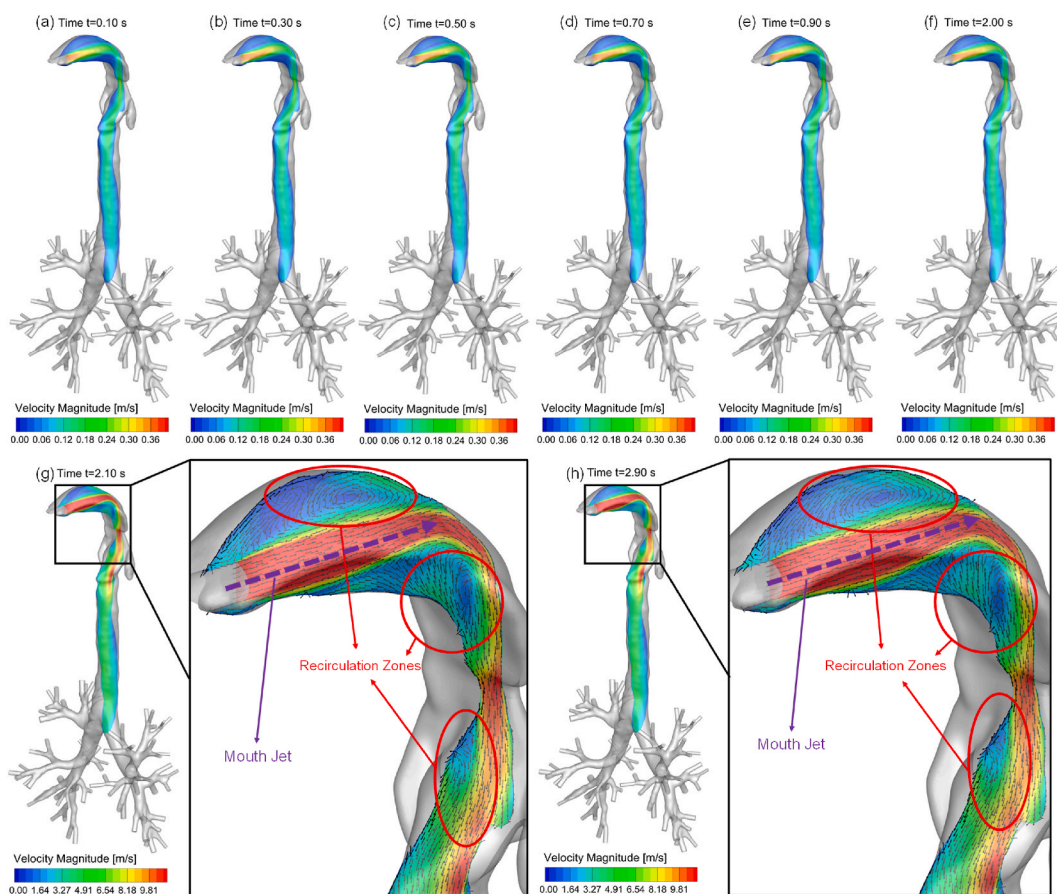
Fig. 7. Evolvement of the airflow velocity magnitude contour and vector field at the sagittal plane of the human respiratory system of the Case 2B with 18.3 ml/s during puffing and a follow-up inhalation flow rate equal to 60 L/min for remaining duration: (a) t = 0.10 s, (b) t = 0.30 s, (c) t = 0.50 s, (d) t = 0.70 s, (e) t = 0.90 s, (f) t = 2.00 s, (g) t = 2.10 s, and (h) t = 2.90 s.

4.2. Nicotine vapor mass fraction distributions in the human respiratory system

As the main focus of this CFPD study, nicotine vapor mass fraction distributions are visualized for Case Freebase with Q_{follow} = 30 L/min and Case 2B with Q_{follow} = 60 L/min in Fig. 10 and Fig. 11, respectively. It can be observed that during the puff (see Fig. 10 (a)–(f) and Fig. 11 (a)-(f)), nicotine vapor follows the mouth jet and gradually increases in the mass fraction from the oral cavity to the trachea. It can be observed that due to the strong convection effect induced by the high-velocity mouth jet core, the shape of the high nicotine vapor fraction region is very similar to the high-velocity region. With the time evolution during the puff, nicotine vapor diffuses from the high-velocity jet core to the ambient spaces in the upper airway. No significant differences in nicotine vapor distributions during the puff can be observed between Case Freebase with Q_{follow} = 30 L/min and Case 2B with Q_{follow} = 60 L/min, although the nicotine deposition and absorption fractions are noticeably influenced by the nicotine form (see Section 4.4). During the follow-up inhalations (see Fig. 10 (g)–(l) and Fig. 11 (g)–(l)), it can be observed that the remaining nicotine vapor in the pulmonary route is gradually absorbed by the airway and transport to the deeper lung region. Case 2B with Q_{follow} = 60 L/min (see Fig. 11 (g)–(l)) has faster transport of the nicotine vapor to the deep lung than Case Freebase with Q_{follow} = 30 L/min (see Fig. 10 (g)–(l)), which is mainly due to the stronger convection effect induced by higher Q_{follow} (60 L/min vs. 30 L/min). Based on such observation, it is evident that stronger follow-up inhalation can enhance the available dose of nicotine vapor in the deeper lung.

4.3. EC droplet deposition patterns in the human respiratory system

Since EC aerosols have droplets inhaled in addition to vapors, the droplet deposition patterns for cases with different nicotine forms, acid types, acid levels, PG/VG ratios, initial droplet diameters, and follow-up inhalation flow rates are shown in Fig. 12 (a)-(j). Droplets were colored by their diameters when they deposit. Despite the differences in initial EC aerosol characteristics mentioned above, consistent deposition patterns of EC droplets can be observed from the cases shown in Fig. 12 (a)–(j). Specifically, concentrated droplet depositions can be found near the glottis region, led by the interception and dispersion effect due to the sudden contraction and expansion near this region. In the TB tree, more droplets deposit at the bifurcating points in each generation. Furthermore, it is
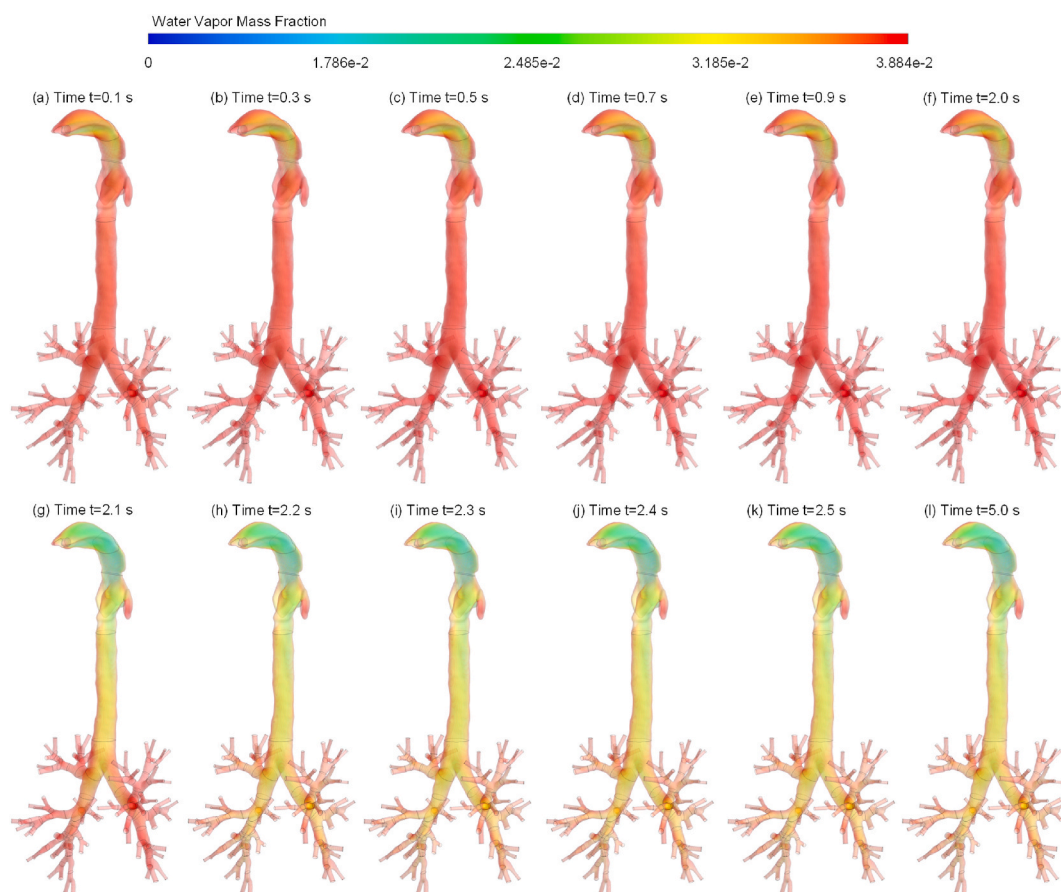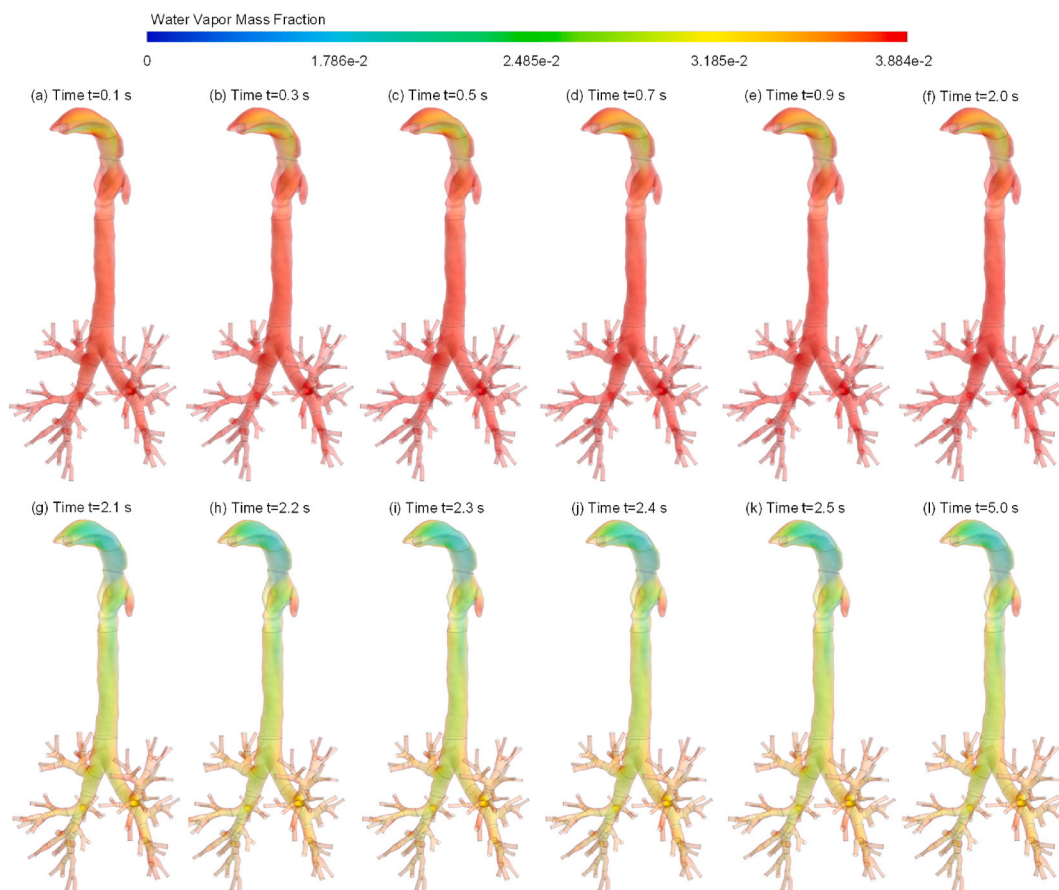
Fig. 8. Evolvement of the water vapor mass fraction in the human respiratory system of the freebase nicotine case with 18.3 ml/s during puffing and a follow-up inhalation flow rate equal to 30 L/min for remaining duration: (a) t = 0.10 s, (b) t = 0.30 s, (c) t = 0.50 s, (d) t = 0.70 s, (e) t = 0.90 s, (f) t = 2.00 s, (g) t = 2.10 s, (h) t = 2.20 s, (i) t = 2.30 s, (j) t = 2.40 s, (k) t = 2.50 s, and (l) t = 5.00 s.

interesting that for all cases shown in Fig. 12 (a)–(j), deposited droplet diameters did not show a significant increase or decrease along with the deposition site moving downstream. This is because of the combined effect of water vapor condensation, PG evaporation, nicotine evaporation, and VG evaporation. Specifically, Most droplets deposited at locations farther away from the mouth should have a longer residence time in the pulmonary route, submerged in higher RH, and thereby have more mass of water condensation compared with droplets deposited at locations closer to the mouth. Meanwhile, longer residence time will also lead to higher mass loss of the droplets due to the evaporation of PG, nicotine, and VG. Therefore, the combined effect of the condensation and evaporation for droplets deposited at different airway locations varied the mass and diameter changes in a similar manner. It can also be observed from Fig. 12 (a)–(j) that the influence of initial EC aerosol characteristics on droplet diameter distributions and deposition patterns is not significant, on the condition that coagulation was not simulated (see Section 6). More details can be found in Sections 4.4-4.7.

### 4.4. Effect of nicotine form, acid type, and acid level

To investigate how nicotine form, acid type, and acid level can influence the EC aerosol transport, phase change, deposition, and absorption, Fig. 13 (a)–(d) compare the deposited droplet diameters, species liquid-vapor phase change percentages, nicotine uptake fractions, and droplet deposition regional distributions among 5 cases, i.e., Case Freebase, Case 1L, Case 2L, Case 1B, and Case 2B, with $d_{d,ini} = 800$ nm and $Q_{follow} = 30$ L/min. The details of initial EC aerosol compositions for those cases can be found in Table 3. It is worth mentioning that the acid/nicotine ratio was weight percentages, used as the parameter for determining the level of protonation. Lower activity coefficients (see Table 3) indicate a lower vapor pressure for nicotine. The evaporation phase change percentage is calculated by species mass evaporated/total mass of that species initially in EC droplets. Since there is no water in the EC droplets initially, water condensation percentage is calculated based on the water vapor mass condensed/total mass of droplets inhaled into the human respiratory system during the single puff simulated for all cases. The same calculation of species liquid-vapor phase change percentages was also performed for Figs. 14–16. All cases shown in Fig. 13 (a)–(d) used otherwise identical formulations of 3% nicotine by mass and a PG/VG ratio of 50:50. Together with Figs. 7–12, the influence of nicotine form, acid type, and acid level are discussed in this section.

It can be observed from Fig. 13 (a) that nicotine form, acid type, and acid level (i.e., acid/nicotine ratio) do not have a significant

Fig. 9. Evolvement of the water vapor mass fraction in the human respiratory system of the Case 2B with 18.3 ml/s during puffing and a follow-up inhalation flow rate equal to 60 L/min for remaining duration (a) t = 0.10 s, (b) t = 0.30 s, (c) t = 0.50 s, (d) t = 0.70 s, (e) t = 0.90 s, (f) t = 2.00 s, (g) t = 2.10 s, (h) t = 2.20 s, (i) t = 2.30 s, (j) t = 2.40 s, (k) t = 2.50 s, and (l) t = 5.00 s.

influence on deposited droplet diameter ranges from mouth to G10. This is due to the fact that nicotine form, acid type, and acid level only have a noticeable influence on nicotine evaporation rate, but a negligible influence on the rates of PG evaporation, VG evaporation, and water condensation, which can be found in Fig. 13 (b). Specifically, Fig. 13 (b) shows that freebase nicotine (i.e., Case Freebase) has the highest percentage magnitude of nicotine liquid-vapor phase change compared with the other 4 cases with nicotine salts, which is approximately 10%. It is worth mentioning that negative percentages in Fig. 13 (b) represent evaporation, while positive percentages mean condensation. It can also be found that with the increase in acid/nicotine ratio (i.e., Case 1B vs. Case 2B or Case 1L vs. Case 2L), the nicotine evaporation rate was reduced. With the same acid/nicotine ratio (e.g., Case 2B vs. Case 2L or Case 1B vs. Case 1L), using benzoic acid can reduce the nicotine evaporation rate more than using lactic acid. Comparisons between freebase nicotine are made against both lactic acid protonated nicotine, as well as benzoic acid, protonated nicotine. Such an observation is because that benzoic acid is a stronger acid than lactic acid. It protonated more of the present nicotine in those cases, which caused less nicotine to evaporate compared to the lactic acid cases. These results follow the expectations from experiments and theory (Pichelstorfer et al., 2016). The higher amount of acid in Case 2B and Case 2L serves to protonate that nicotine which reduces the evaporation rate. Moreover, PG evaporation, VG evaporation, and water condensation did not have noticeable changes with the change of nicotine form, acid type, and acid level. Since nicotine liquid only accounts for 3% of the initial EC droplet mass, which has a noticeable liquid-vapor phase change rate with the variation in nicotine form, acid type, and acid level, final deposited droplet diameter ranges should not be influenced significantly, as shown in Fig. 13 (a). Fig. 13 (c) shows how nicotine liquid deposition, vapor absorption, and total nicotine uptake were influenced. It can be found that most nicotine uptake is due to nicotine vapor absorption instead of nicotine-containing droplet deposition. It can be observed that nicotine liquid deposition via droplets has not been significantly influenced by nicotine form, acid type, and acid level. In contrast, with the increase in activity coefficient γ_s for less pronated nicotine, the nicotine vapor absorption in the human respiratory system also increased. Specifically, the increase in nicotine vapor absorption shown in Fig. 13 (c) indicates that using pronated nicotine can reduce the nicotine liquid evaporation, thereby reducing the nicotine vapor concentration and absorption from mouth to G10. As a result, using pronate nicotine can deliver more nicotine into deeper lungs beyond G10. Additionally, Fig. 13 (d) shows the regional deposition fractions of inhaled EC droplets for Cases Freebase, 1L, 2L, 1B, and 2B. No significant deposition fraction change was caused by the variations in nicotine form. Together with the observations based on
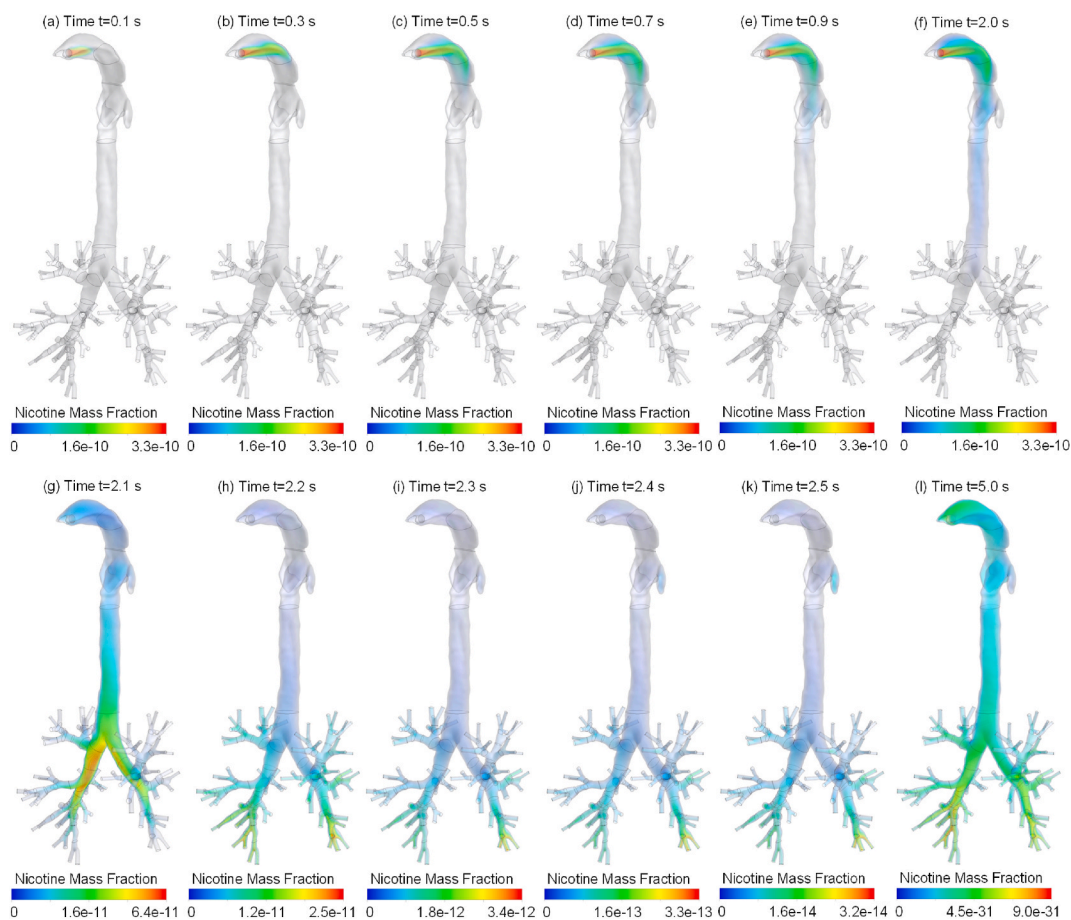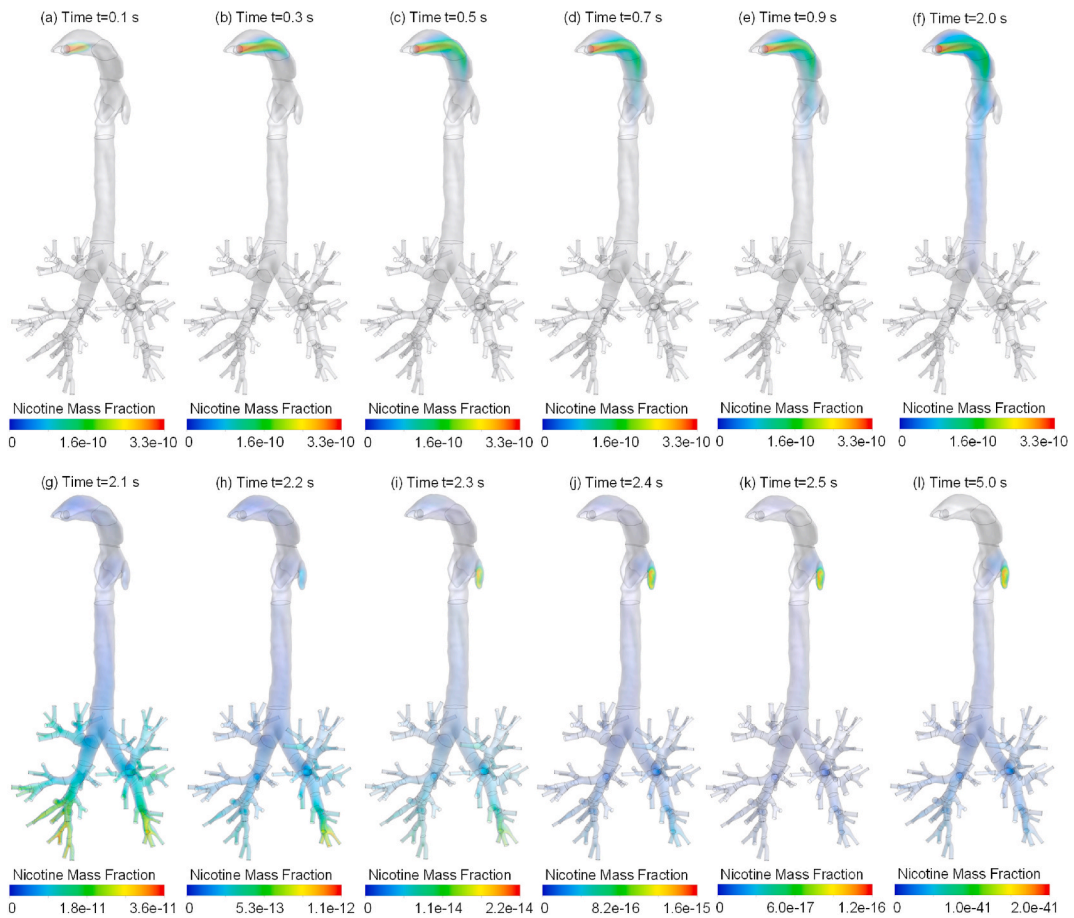
Fig. 10. Evolvement of the nicotine vapor mass fraction in the human respiratory system of the freebase nicotine case with 18.3 ml/s during puffing and a follow-up inhalation flow rate equal to 30 L/min for remaining duration (a) t = 0.10 s, (b) t = 0.30 s, (c) t = 0.50 s, (d) t = 0.70 s, (e) t = 0.90 s, (f) t = 2.00 s, (g) t = 2.10 s, (h) t = 2.20 s, (i) t = 2.30 s, (j) t = 2.40 s, (k) t = 2.50 s, and (l) t = 5.00 s.

Figs. 7–12, it can be concluded that nicotine form, acid type, and acid level have a noticeable influence on nicotine evaporation and vapor absorption but an insignificant effect on EC droplet size change and deposition location and doses.

4.5. Effect of PG/VG ratio

To further influence the initial EC aerosol composition, two sets of cases with different PG/VG ratios were simulated and compared in Fig. 14 (a)–(d). The first set is based on Case Freebase, and the second set is based on Case 2B. Three initial PG/VG ratios in e-liquid were used, i.e., 25:75, 50:50, and 75:25, for both freebase and protonated nicotine forms. Since it has been found from Fig. 13 (a) that droplet size change dynamics are similar between Case Freebase and Case 2B, Fig. 14 (a) only plots the deposited droplet diameters with protonated nicotine case set. Specifically, Fig. 14 (a) shows with the increase in PG/VG ratio in initial EC droplet composition, the mean and minimum deposited droplet diameters decrease, while the maximum deposited droplet diameters are similar. Compared with Fig. 13, the diameter differences between protonated and freebase nicotine are much smaller than the difference between PG/VG ratios. This is due to the fact that while nicotine evaporation contributes to the diameter change, the principal contributor is the PG evaporation and water condensation. However, the faster reduction in droplet diameters with a higher PG/VG ratio is mainly due to the less water condensation during their transport instead of variations in PG evaporation, which can be found in Fig. 14 (b) and (c). Specifically, Fig. 14 (b) and (c) show that the PG evaporation percentage does not change significantly with the PG/VG ratio alternation, in which water condensation decreases with the increase in PG/VG ratio. Indeed, with the same diameter, droplets with a higher PG/VG ratio have more PG liquid mass in the initial droplets. Therefore, droplets with a higher PG/VG ratio will have a faster PG evaporation rate than droplets with a lower PG/VG ratio. With the faster PG evaporation rate, the droplet diameter reduction is also more rapid, indicating the droplet surface curvature increase is also faster. With the higher droplet surface curvature, the Kelvin effect is stronger for droplets with an initially high PG/VG ratio, indicating less water condensation is needed to reach the saturation equilibrium at the droplet surface (Lewis, 2006). Fig. 14 (b) and (c) also show that increasing PG/VG ratio will slightly decrease the nicotine evaporation rate for both freebase nicotine and protonated nicotine. It is because of the difference in nicotine volatility

Fig. 11. Evolvement of the nicotine vapor mass fraction in the human respiratory system of the Case 2B with 18.3 ml/s during puffing and a follow-up inhalation flow rate equal to 60 L/min for remaining duration: (a) t = 0.10 s, (b) t = 0.30 s, (c) t = 0.50 s, (d) t = 0.70 s, (e) t = 0.90 s, (f) t = 2.00 s, (g) t = 2.10 s, (h) t = 2.20 s, (i) t = 2.30 s, (j) t = 2.40 s, (k) t = 2.50 s, and (l) t = 5.00 s.

dependent on the PG/VG ratio, which causes variations in the nicotine liquid evaporation from the droplets (see Eqs. (21)-(23)). Fig. 14 (d) shows that with the increase in PG/VG ratio, nicotine uptake from mouth to G10 decreases, which is dominantly determined by the decrease in nicotine vapor absorption. Therefore, it can be concluded that a higher initial PG/VG ratio in the e-liquid can noticeably decrease the deposited EC droplet size, reduce nicotine evaporation, lower the nicotine uptake from mouth to G10, and enhance the nicotine delivery to the deeper lung. Additionally, it can be observed that the influence of the PG/VG ratio on droplet deposition patterns is not significant from Fig. 12 (c), (f), and (g).

4.6. Effect of initial droplet diameter

In previous sections, initial EC droplet diameters for the cases compared were 800 nm. To investigate how initial droplet size can influence the EC aerosol transport, phase change, deposition, and absorption in the human respiratory system, additional Case 2B simulations were run with 500 nm and 1000 nm as the initial EC droplet diameters and all other parameters identical. The comparisons of the three cases are shown in Fig. 15 (a)–(d). These cases used a benzoic acid mixture with 3% nicotine, PG/VG ratio = 50:50 (α = 0.5), acid/nicotine ratio = 1:1 (β = 1). Fig. 15 (a) shows that with the increase in initial droplet diameter, the average growth ratio (GR) for the deposited droplets increased. GR is defined by the ratio of the final droplet diameter and initial droplet diameter. Interestingly, with $d_{d,ini}$ = 500 nm, the average droplet diameter becomes smaller rather than larger than the initial diameter. Such a trend is majorly due to the increased water condensation (see Fig. 15 (b)) because of the reduced Kelvin effect (Lewis, 2006). Fig. 15 (b) also shows that nicotine and PG evaporation rate was reduced with the increase in initial droplet diameter $d_{d,ini}$, which is the other factors that increase the droplet GR as shown in Fig. 15 (a). Fig. 15 (c) presents how $d_{d,ini}$ influences nicotine liquid deposition, vapor absorption, and total uptakes in the human respiratory system covering from mouth to G10. The comparison shows that the cases with larger $d_{d,ini}$ have a slightly higher deposition fraction than that of the smaller $d_{d,ini}$. The reasoning for this difference is that the smaller droplet sizes contain less mass and can more easily follow the primary phase flow to avoid inertial impaction-induced depositions. However, despite having a lower deposited mass, the case with $d_{d,ini}$ = 500 nm experienced the most nicotine absorption of all cases
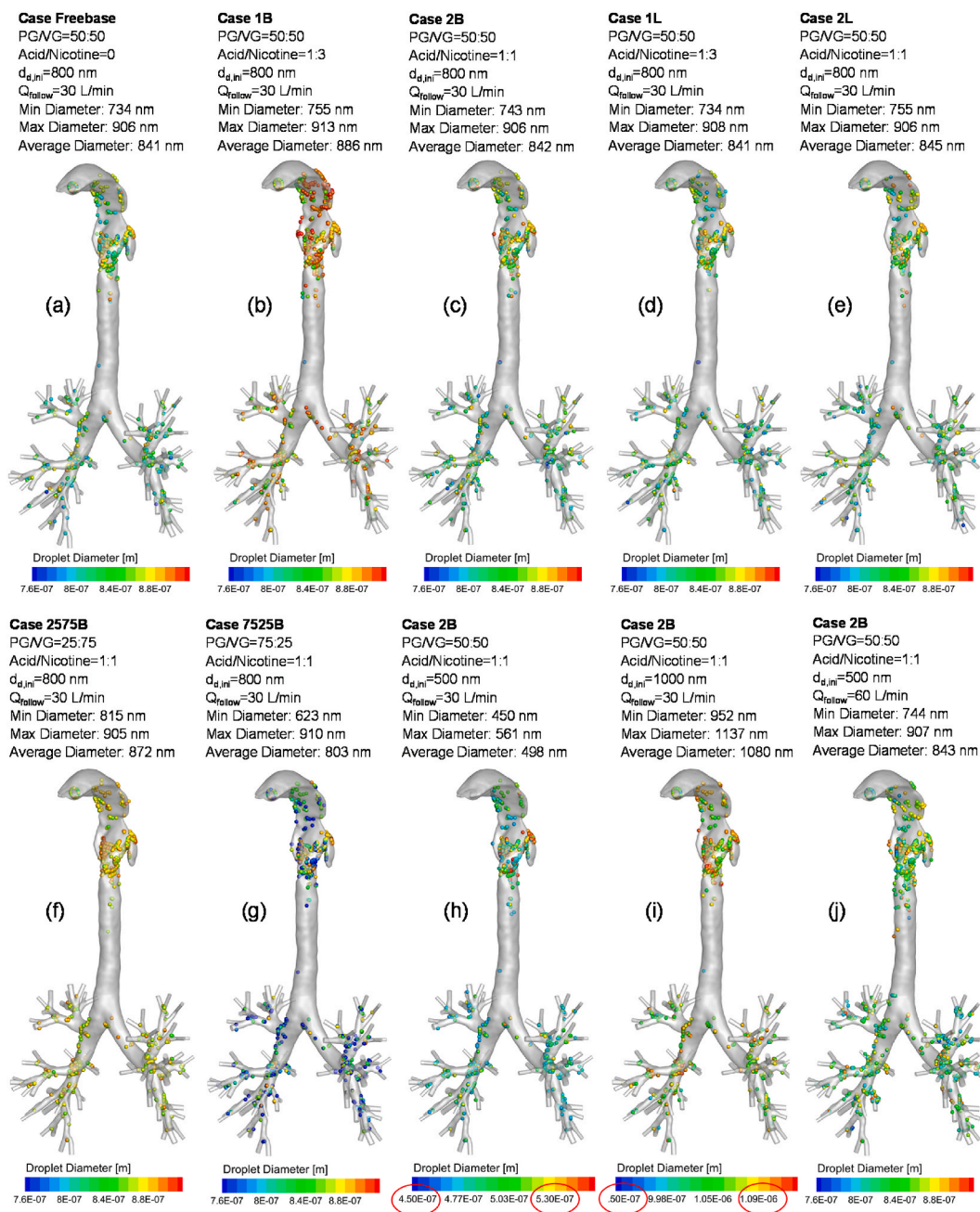
Fig. 12. EC droplet deposition patterns colored by droplet diameters ($d_{d,ini}$ = 800 nm and Q_{follow} = 30 L/min unless otherwise noted): (a) Case Freebase, (b) Case 1B, (c) Case 2B, (d) Case 1L, (e) Case 2L, (f) Case 2575B, (g) Case 7525B, (h) Case 2B with $d_{d,ini}$ = 500 nm, (i) Case 2B with $d_{d,ini}$ = 1000 nm, and (j) Case 2B with Q_{follow} = 60L/min.

due to the high absorption of vapor phase nicotine, which is because of the highest nicotine evaporation shown in Fig. 15 (b). Fig. 15 (d) further visualizes regional nicotine uptake fractions in the mouth-to-trachea and trachea-to-G10 regions. With the stronger inertial impaction for larger droplets, the nicotine liquid uptake fraction in the mouth-to-trachea region increases with the increase in $d_{d,ini}$ because of the higher number of deposited droplets in this region. However, it can be observed that influence of initial droplet diameter on droplet local deposition patterns is not significant from Fig. 12 (c), (h), and (i). In summary, among the three initial droplet diameters investigated in this study, larger $d_{d,ini}$ = 1000 nm will reduce nicotine vapor absorption and total nicotine uptake from mouth to G10, thereby enhancing the availability of nicotine to the deeper lung. Initial droplet diameter did not significantly influence the EC droplet deposition patterns or regional deposition fractions.
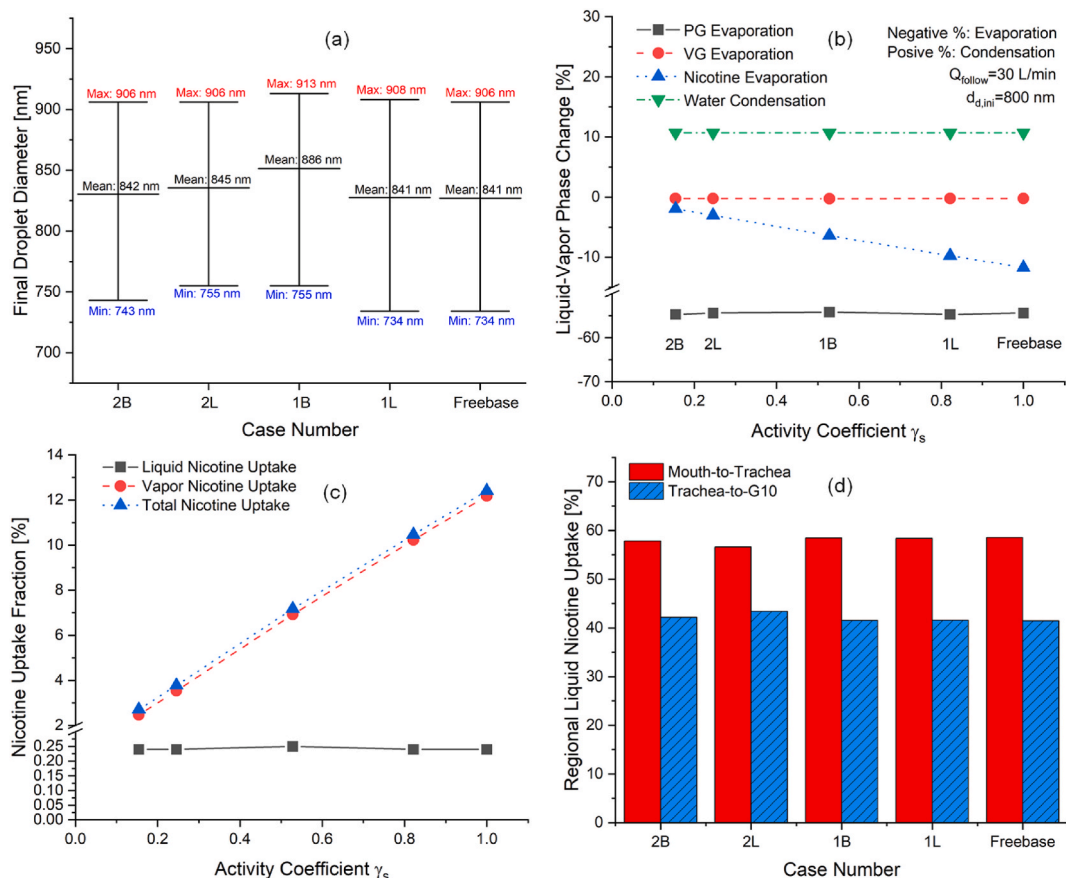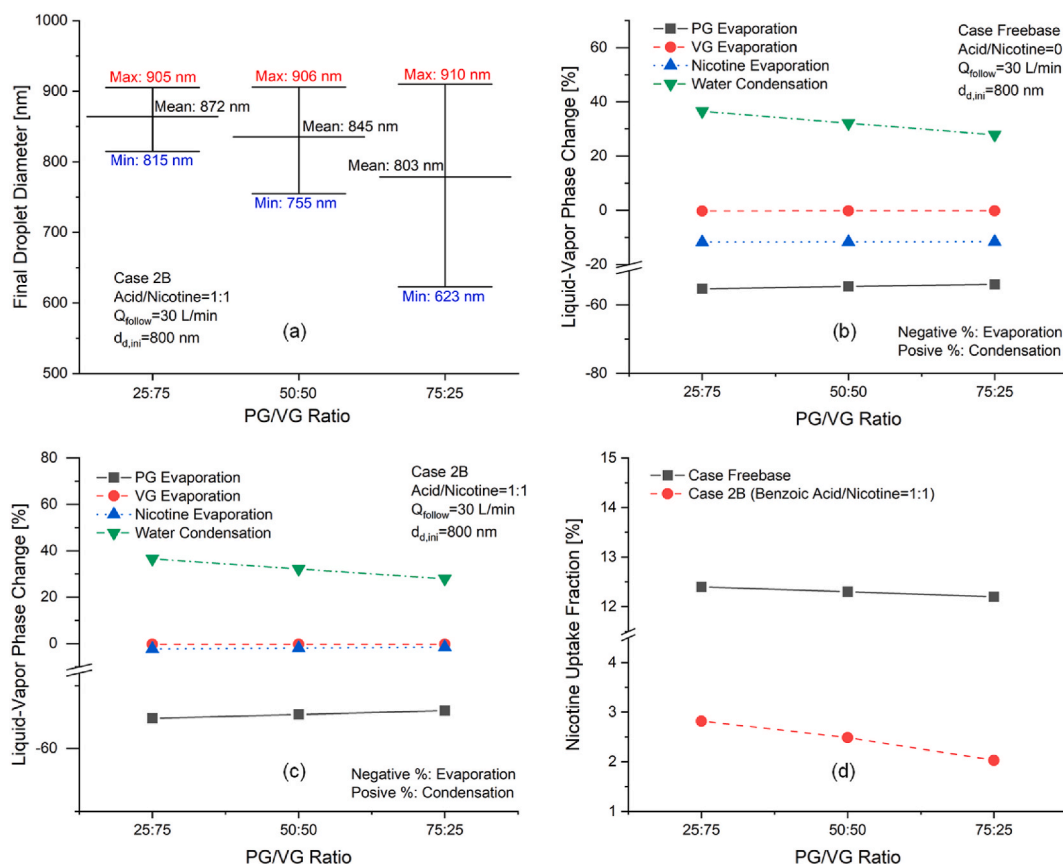
Fig. 13. Influence of nicotine form, acid type, and acid level of e-liquid on (a) droplet size change dynamics, (b) liquid-vapor phase change percentages, (c) liquid and vapor nicotine uptakes in the subject-specific human respiratory system, and (d) regional liquid nicotine uptake fractions.

4.7. Effect of follow-up inhalation flow rate

To partially investigate how breathing style may influence the EC aerosol fate in human respiratory system, two inhalation flow rates following the puff were simulated using Case 2B (i.e., Q_{follow} = 30 L/min and 60 L/min). Specifically for this investigation, the same 18.3 ml/s flow rate was used for the puff, followed by different intensities of inhalation. The influence of Q_{follow} on pulmonary airflow and vapor transport dynamics has been discussed in Sections 4.1 and 4.2. Fig. 16 (a)–(d) visualized droplet diameter change, nicotine vapor phase change, liquid and vapor nicotine uptake, and liquid nicotine regional deposition fractions between the two cases with different follow-up flow rates. It can be found from Fig. 16 (a) that deposited droplet diameters was not significantly influenced by Q_{follow}, although that Q_{follow} has noticeably altered transient RH distributions in the human respiratory system (see Figs. 8 and 9). Indeed, since the droplets entered the mouth earlier than the start of the follow-up inhalation, the RH differences caused by different Q_{follow} values were always delayed and only can influence the region upstream from the droplet locations. Therefore, although RH should dominantly affect the EC droplet size change, it did not have a noticeable impact due to the reason mentioned above. Fig. 16 (b) shows that Q_{follow} has negligible influence on nicotine evaporation. In addition, Fig. 16 (c) and (d) demonstrate that increasing Q_{follow} can enhance the total droplet deposition in the subject-specific respiratory system used in this study, while the regional deposition fractions are similar. This is due to the overall enhanced inertial impaction with higher Q_{follow}. It can also be observed from Fig. 16 (c) that nicotine vapor absorption is also higher when Q_{follow} is increased, which is due to the enhanced convection of nicotine vapor into the TB tree. This observation is consistent with existing studies (Haghnegahdar et al., 2018).

5. Conclusions

In summary, a CFPD model based on species transport and DPM has been developed, calibrated, and validated to quantify how initial e-liquid composition and inhalation style can influence the transport, evaporation/condensation, and deposition/absorption of inhaled multi-component EC aerosol in a subject-specific human respiratory system. The CFPD model can capture the influence of nicotine forms on the alteration of evaporation/condensation characteristics of EC aerosols. The CFPD model is potentially beneficial to noninvasively provide quantitative evidence for more insightful premarket evaluation of EC products to ensure their safety and

Fig. 14. Influence of initial PG/VG ratio of e-liquid on (a) droplet size change dynamics, (b) liquid-vapor phase change percentages (Case Freebase), (c) liquid-vapor phase change percentages (Case 2B with Benzoid Acid/Nicotine Ratio = 1:1), and (d) nicotine uptakes in the subject-specific human respiratory system.

effectiveness. Key conclusions are listed below.

(1) Nicotine form, acid type, and acid level have a noticeable influence on nicotine evaporation and vapor absorption but have an insignificant effect on EC droplet size change and deposition location and doses. Compared with freebase nicotine, acid protonation on nicotine (e.g., nicotine salt) can reduce nicotine volatility, lower the nicotine loss from mouth to G10, and deliver more nicotine into deeper airways beyond G10. Benzoic acid modified formulations retain more nicotine in the liquid phase than freebase and lactic acid forms. Lactic acid is less strong and retains less liquid phase nicotine at the same weight fraction as benzoic acid.

(2) Higher initial PG/VG ratio in the e-liquid can noticeably decrease the deposited EC droplet size with significantly reduced water condensation, slightly reduced PG and nicotine evaporations, lower the nicotine uptake from mouth to G10, and enhance the nicotine delivery to the deeper lung. However, the influence of the PG/VG ratio on droplet deposition patterns is not significant.

(3) Larger initial EC droplet diameter (i.e., $d_{d,ini} = 1000$ nm vs. $d_{d,ini} = 500$ nm or 800 nm) will reduce nicotine evaporation, vapor absorption and total nicotine uptake from mouth to G10, and enhance the availability of nicotine to the deeper lung. Initial EC droplet diameter did not significantly influence the EC droplet deposition patterns or regional deposition fractions.

(4) With the same puff, an increase in the follow-up inhalation flow rate from 30 L/min to 60 L/min can enhance the total droplet deposition and nicotine vapor absorption in the subject-specific respiratory system due to the enhanced inertial impaction and convection to TB tree.

6. Limitation of the study and future work

As the limitations of this numerical study, the assumptions and simplifications are

(1) No PG vapor were assumed in the initial EC aerosols entering the mouth;
(2) Constant flow rates were used for the puff and follow-up inhalations;
(3) Uniform pressure outlet were applied at all airway terminals;
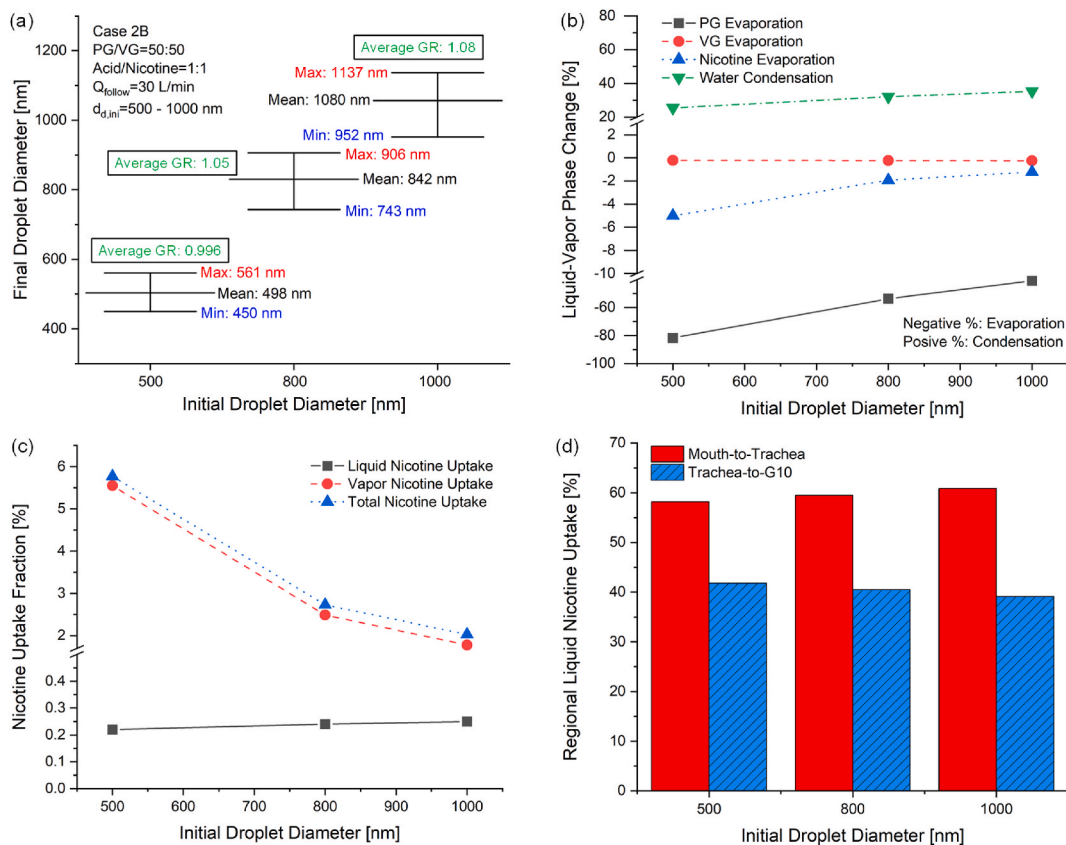
Fig. 15. Influence of initial droplet diameter on (a) droplet size change dynamics, (b) liquid-vapor phase change percentages, (c) liquid and vapor nicotine uptakes in the subject-specific human respiratory system, and (d) regional liquid nicotine uptake fractions.

(4) The breath-holding was not modeled between a puff and the follow-up inhalation-exhalation cycle;

(5) Monodispersed EC droplets were assumed, which are represented by the mean diameter;

(6) Coagulation between EC droplets was neglected in this CFPD model; and

(7) The glottis and TB tree of the subject-specific human respiratory system was assumed to be static without physiologically realistic expansion/contraction motion.

Accordingly, future work on multi-component EC aerosol transport dynamics predictions will include

(1) Adding PG vapor in the initial EC aerosols entering the mouth inlet;

(2) Employing subject-specific transient waveforms of puffing, holding, and the follow-up inhalation-exhalation in CFPD simulations;

(3) Collaborating with *in vitro* and *in vivo* experiments to obtain non-uniform pressure outlet or flow rate outlet conditions to replace the simplified uniform pressure outlet boundary conditions;

(4) Using polydisperse initial EC droplet size distributions to obtain simulation results that will be compared with the monodisperse simulation results to determine whether monodisperse simulations can represent the more realistic polydisperse cases;

(5) Developing new user-defined functions (UDFs) to model the coagulations between EC droplets during their transport to enhance the current CFPD modeling realism;

(6) Investigating how disease-specific lung airway and glottis deformation kinematics can influence the inhaled nicotine distributions using the elastic lung modeling framework (Zhao, Feng, Koshiyama, & Wu, 2021); and

(7) Quantifying the pharmacokinetics of nicotine after deposition/absorption in the human body using a similar modeling framework to the in-house CFPD- Physiologically based toxicokinetics (PBTK) models (Haghnegahdar et al., 2018).

Declaration of competing interest

The authors declare that they have no known competing financial interests or personal relationships that could have appeared to influence the work reported in this paper.
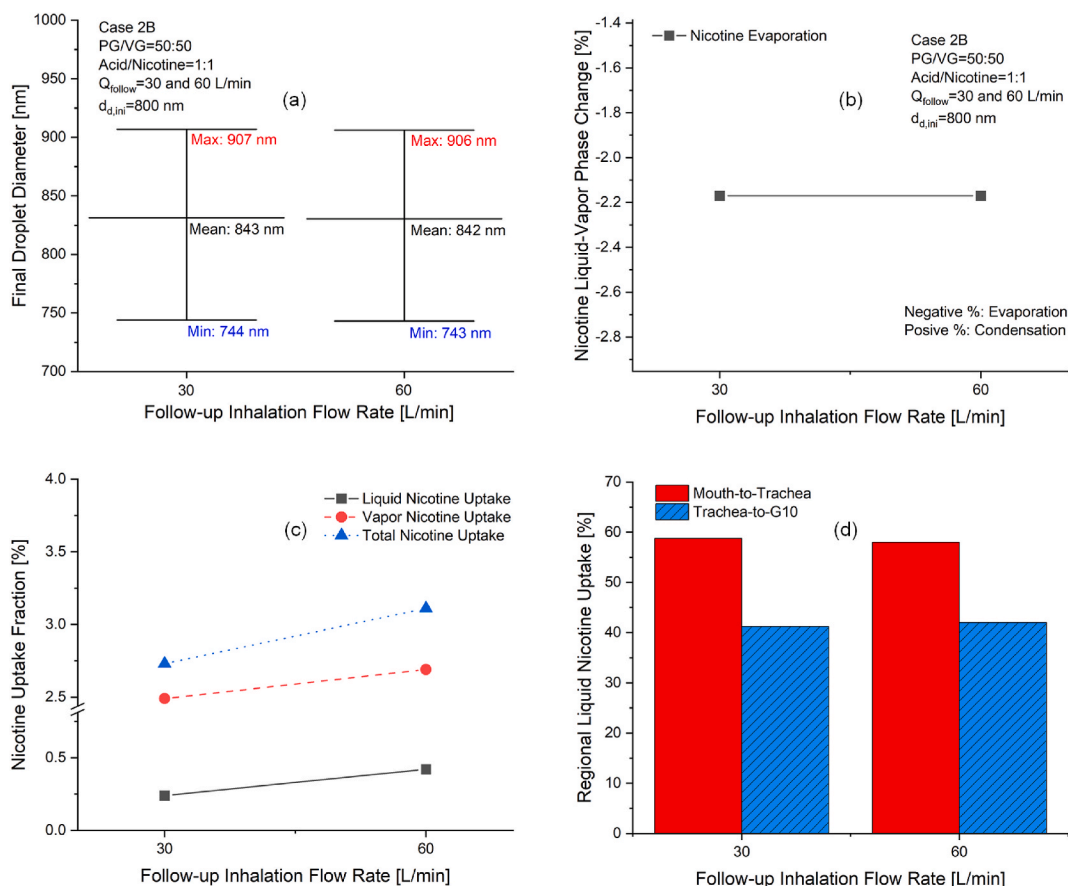
Fig. 16. Influence of follow-up inhalation flow rate Q_{follow} on (a) droplet size change dynamics, (b) liquid-vapor phase change percentages, (c) liquid and vapor nicotine uptakes in the subject-specific human respiratory system, and (d) regional liquid nicotine uptake fractions.

Data availability

Data will be made available on request.

Acknowledgment

Appendix A. Correction Factor (CF) Calibration

1. Introduction

A Correction Factor (CF) was introduced to revise the evaporation/condensation rate due to the differences of e-cigarette (EC) aerosol droplets of 1.68×10^6 used in the simulation compared to real e-cigarette (EC) aerosols. Specifically, in real EC aerosols, droplet number density is estimated to be approximately $2.5 \times 10^7 \pm 7 \times 10^6$ droplets/puff with a mass of 113 ± 42 μg/puff (Li et al., 2020). The CF was determined by comparing the nicotine retention data in a denuder between the simulations and in-house experimental data.

2. Denuder Geometry and Mesh

A 3D digital denuder (see Fig. A1) was constructed with the same geometric dimensions as the in-house experimental setup. The

tubular denuder is 1.5 m long and has a hydraulic diameter of 0.008 m. A structured mesh was generated, containing 146,020 hex elements, 443,212 faces, and 151,350 nodes.

3. Validation of Nicotine Vapor Transport and Absorption in Denuder

Due to the various gas phase nicotine diffusivities in literature, the diffusivity was first calibrated from the absorption in a denuder based on the validated Lipowicz-Paide (L-P) model (Lipowicz & Piadé, 2004). This model represents the gas phase nicotine which deposits on the wall and does not consider the radial diffusion of droplets, so there is no droplet deposition in the L-P model. The model was formulated from a coupled set of differential equations for radial diffusion of a gaseous species and laminar flow in a denuder. The L-P model considers a constant volume fraction of droplets, whereas the simulation accounts for the changing size of droplets. As shown in Fig. A2, the CFPD simulation results of nicotine retention agree with the prediction using the L-P model well using nicotine diffusivity equal to 6.5e-6 m^2/s at 25 ℃.

4. CF Calibration

CF was calibrated to match the results of an experimental denuder tube setup where nicotine-containing droplets are drawn through a cylindrical tube to measure the evaporation rate and diffusivity of nicotine. CFPD simulations were run with CF values from 0.0005 to 0.005, where a smaller value represents a lower vaporization rate for all species. The nicotine inlet flow rate was set at 0.5 L/min. The EC droplet diameter was 800 nm. The nicotine liquid-gas partition used in this case was 90% liquid and 10% vapor, with the gas phase mass added to the entering air-nicotine vapor mixture. The nicotine activity coefficient reflects a 1:1 benzoic acid to nicotine ratio, which is identical to the in-house experimental setup. From the nicotine penetration comparison with experimental data shown in Fig. A3, CF = 0.005 can provide an accurate prediction of nicotine penetration (i.e., 87.92%) at 0.3 m denuder cross-section from the inlet, which indicates the accurate prediction of nicotine evaporation/condensation rate with the reduced number density of EC droplets.
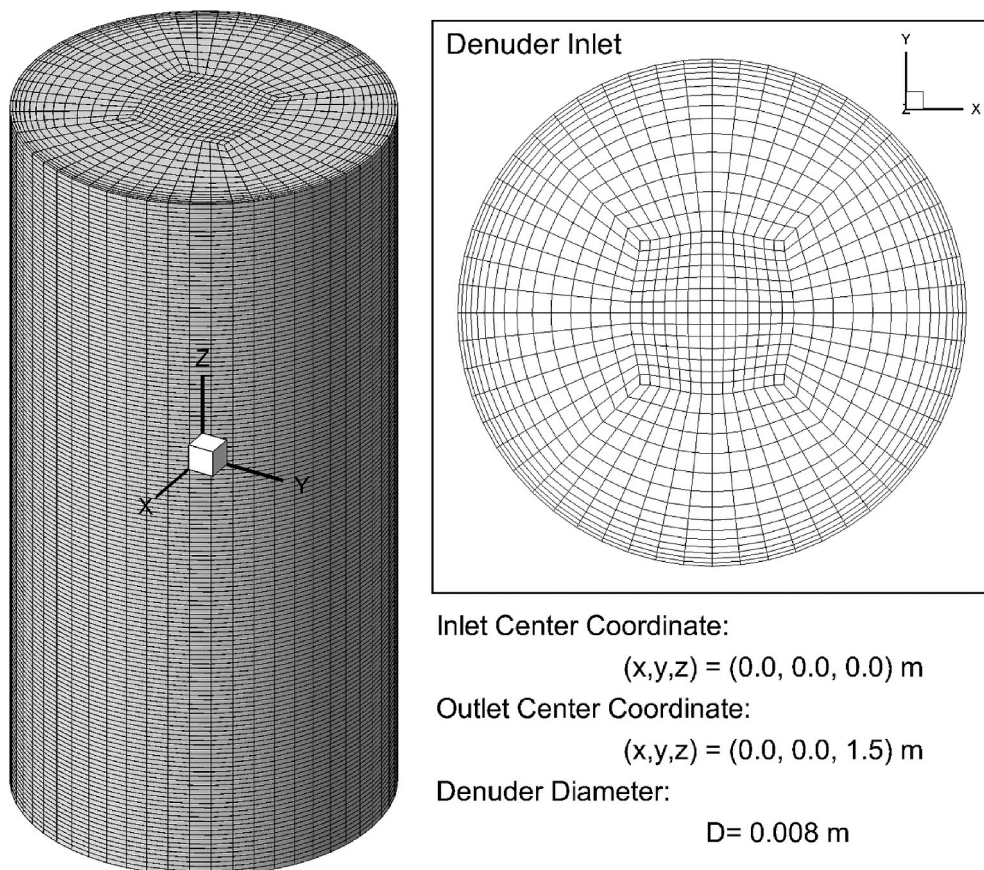

Inlet Center Coordinate:
(x,y,z) = (0.0, 0.0, 0.0) m
Outlet Center Coordinate:
(x,y,z) = (0.0, 0.0, 1.5) m
Denuder Diameter:
D= 0.008 m

Fig. A1. Denuder Geometry and Mesh Details (Z-to-X and Z-to-Y scales were adjusted for better visualization purpose).
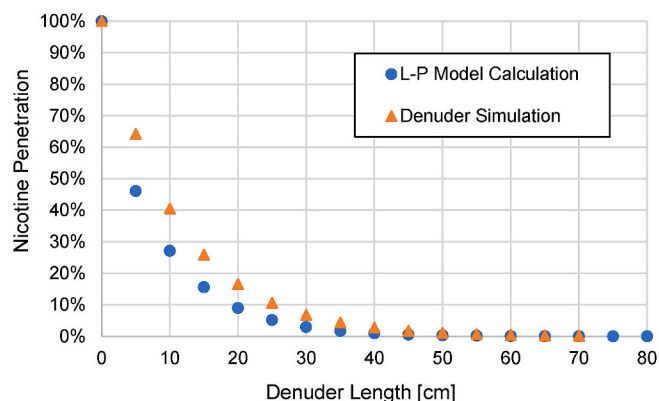
Fig. A2. Penetration efficiency vs. denuder length predicted by the CFPD model and L-P model.
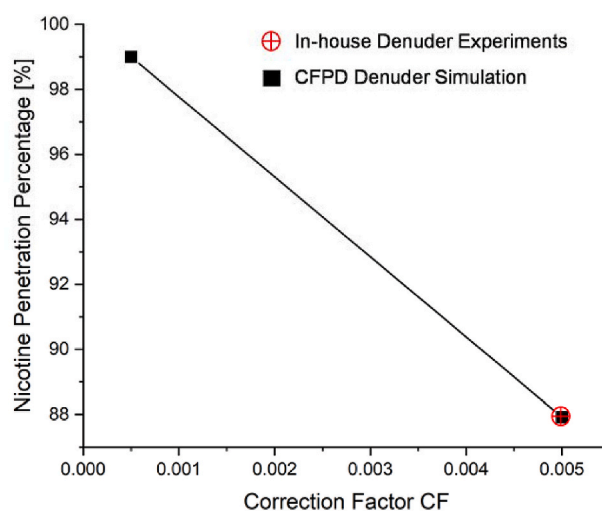

Fig. A3. Comparisons of nicotine penetration percentages between CFPD simulations using different CF values and in-house denuder experimental data.

References

Asgari, M., Lucci, F., & Kuczaj, A. K. (2021). Multispecies aerosol evolution and deposition in a human respiratory tract cast model. *Journal of Aerosol Science, 153,* Article 105720.

Asgharian, B., Rostami, A. A., Price, O. T., & Pithawalla, Y. B. (2018). Regional deposition of inhaled aerosol constituents from Electronic Nicotine Delivery Systems (ENDS) in the respiratory tract. *Journal of Aerosol Science, 126,* 7–20.

Cohen, J. E., Hardesty, J. J., Nian, Q., Crespi, E., Sinamo, J. K., Kennedy, R. D., … Breland, A. B. (2022). Combinations of electronic nicotine delivery system device and liquid characteristics among U.S. adults. *Addictive Behaviors, 135,* Article 107441.

David, G., Parmentier, E. A., Taurino, I., & Signorell, R. (2020). Tracing the composition of single e-cigarette aerosol droplets in situ by laser-trapping and Raman scattering. *Scientific Reports, 10*(1), 1–8.

Duell, A. K. (2019). *Analysis of E-cigarette liquids and aerosols by NMR spectroscopy: Compositions, boiling points, and degradation profiles*.

Feng, Y., Kleinstreuer, C., Castro, N., & Rostami, A. (2016). Computational transport, phase change and deposition analysis of inhaled multicomponent droplet–vapor mixtures in an idealized human upper lung model. *Journal of Aerosol Science, 96,* 96–123.

Feng, Y., Kleinstreuer, C., & Rostami, A. (2015). Evaporation and condensation of multicomponent electronic cigarette droplets and conventional cigarette smoke particles in an idealized G3–G6 triple bifurcating unit. *Journal of Aerosol Science, 80,* 58–74.

Feng, Y., Zhao, J., Kleinstreuer, C., Wang, Q., Wang, J., Wu, D. H., et al. (2018). An in silico inter-subject variability study of extra-thoracic morphology effects on inhaled particle transport and deposition. *Journal of Aerosol Science, 123,* 185–207.

Fisenko, S. P., Rostami, A. A., Kane, D. B., Pithawalla, Y. B., Maximoff, S. N., Li, W., et al. (2021). Model of aerosol evolution in high supersaturated air-glycerol vapor mixtures. *Aerosol Science and Technology, 55*(8), 871–885.

Glasser, A. M., Collins, L., Pearson, J. L., Abudayyeh, H., Niaura, R. S., Abrams, D. B., et al. (2017). Overview of electronic nicotine delivery systems: A systematic review. *American Journal of Preventive Medicine, 52*(2), e33–e66.

Haghnegahdar, A., Feng, Y., Chen, X., & Lin, J. (2018). Computational analysis of deposition and translocation of inhaled nicotine and acrolein in the human body with e-cigarette puffing topographies. *Aerosol Science and Technology, 52*(5), 483–493.

Haghnegahdar, A., Zhao, J., & Feng, Y. (2019). Lung aerosol dynamics of airborne influenza A virus-laden droplets and the resultant immune system responses: An in silico study. *Journal of Aerosol Science, 134,* 34–55.

Hartmann-Boyce, J., McRobbie, H., Lindson, N., Bullen, C., Begh, R., Theodoulou, A., … Hajek, P. (2021). Electronic cigarettes for smoking cessation. *Cochrane Database of Systematic Reviews, 4*(12), 1465–1858.

Harvanko, A. M., Havel, C. M., Jacob, P., & Benowitz, N. L. (2020). Characterization of nicotine salts in 23 electronic cigarette refill liquids. *Nicotine & Tobacco Research, 22*(7), 1239–1243.

Hinds, W. C., & Zhu, Y. (2022). *Aerosol technology: Properties, behavior, and measurement of airborne particles.* John Wiley & Sons.

John, E., Coburn, S., Liu, C., McAughey, J., Mariner, D., McAdam, K., … Dóbé, S. (2018). Effect of temperature and humidity on the gas–particle partitioning of nicotine in mainstream cigarette smoke: A diffusion denuder study. *Journal of Aerosol Science, 117*, 100–117.

Johnson, N. L., Patten, T., Ma, M., De Biasi, M., & Wesson, D. W. (2022). Chemosensory contributions of E-cigarette additives on nicotine use. *Frontiers in Neuroscience, 16*, Article 893587.

Kiraz, A., Karadağ, Y., & Muradoğlu, M. (2008). Large spectral tuning of a water–glycerol microdroplet by a focused laser: Characterization and modeling. *Physical Chemistry Chemical Physics, 10*(42), 6446–6454.

Lewis, E. R. (2006). The effect of surface tension (Kelvin effect) on the equilibrium radius of a hygroscopic aqueous aerosol particle. *Journal of Aerosol Science, 37*(11), 1605–1617.

Li, W., & Hopke, P. (1993). Initial size distributions and hygroscopicity of indoor combustion aerosol particles. *Aerosol Science and Technology, 19*(3), 305–316.

Li, L., Lee, E. S., Nguyen, C., & Zhu, Y. (2020). Effects of propylene glycol, vegetable glycerin, and nicotine on emissions and dynamics of electronic cigarette aerosols. *Aerosol Science and Technology, 54*(11), 1270–1281.

Lipowicz, P. J., & Piadé, J. J. (2004). Evaporation and subsequent deposition of nicotine from mainstream cigarette smoke in a denuder tube. *Journal of Aerosol Science, 35*(1), 33–45.

Meissner, H. I., Sharma, K., Mandal, R. J., Garcia-Cazarin, M., Wanke, K. L., Moyer, J., et al. (2022). NIH tobacco research and the emergence of tobacco regulatory science. *Nicotine & Tobacco Research, 24*(4), 463–468.

Owotomo, O., & Walley, S. (2022). The youth e-cigarette epidemic: Updates and review of devices, epidemiology and regulation. *Current Problems in Pediatric and Adolescent Health Care*, Article 101200.

Phalen, R. F., Hoover, M. D., Oldham, M. J., Schmid, O., & Golshahi, L. (2021). Anatomical considerations for inhaled aerosol deposition modeling: Methods, applications, challenges and opportunities. *Journal of Aerosol Science, 156*, Article 105786.

Pichelstorfer, L., Hofmann, W., Winkler-Heil, R., Yurteri, C. U., & McAughey, J. (2016). Simulation of aerosol dynamics and deposition of combustible and electronic cigarette aerosols in the human respiratory tract. *Journal of Aerosol Science, 99*, 125–132.

Pichelstorfer, L., Winkler-Heil, R., Boy, M., & Hofmann, W. (2021). Aerosol dynamics simulations of the anatomical variability of e-cigarette particle and vapor deposition in a stochastic lung. *Journal of Aerosol Science, 158*, Article 105706.

Pourhashem, H., Owen, M. P., Castro, N. D., & Rostami, A. A. (2020). Eulerian modeling of aerosol transport and deposition in respiratory tract under thermodynamic equilibrium condition. *Journal of Aerosol Science, 141*, Article 105501.

Richardson, A. (1886). LXXIII.—Determinations of vapour-pressures of alcohols and organic acids, and the relations existing between the vapour-pressures of the alcohols and organic acids. *Journal of the Chemical Society Transactions, 49*, 761–776.

Shamout, M., Wang, P., Wong, F., Chen, W., Kumagai, K., Pérez, J. J., … Herzig, C. (2021). Chemical composition of JUUL pods collected from students in California high schools. *Journal of Adolescent Health, 69*(2), 342–345.

Siitsman, C., Kamenev, I., & Oja, V. (2014). Vapor pressure data of nicotine, anabasine and cotinine using differential scanning calorimetry. *Thermochimica Acta, 595*, 35–42.

Sleiman, M., Logue, J. M., Montesinos, V. N., Russell, M. L., Litter, M. I., Gundel, L. A., et al. (2016). Emissions from electronic cigarettes: Key parameters affecting the release of harmful chemicals. *Environmental Science and Technology, 50*(17), 9644–9651.

Smolík, J., Džumbová, L., Schwarz, J., & Kulmala, M. (2001). Evaporation of ventilated water droplet: Connection between heat and mass transfer. *Journal of Aerosol Science, 32*(6), 739–748.

Spahn, J. E., Stavchansky, S. A., & Cui, Z. (2021). Critical research gaps in electronic cigarette devices and nicotine aerosols. *International Journal of Pharmaceutics, 593*, Article 120144.

Stefaniak, A. B., Ranpara, A. C., Virji, M. A., & LeBouf, R. F. (2022). Influence of E-liquid humectants, nicotine, and flavorings on aerosol particle size distribution and implications for modeling respiratory deposition. *Frontiers in Public Health, 10*, 782068.

Stull, D. R. (1947). Vapor pressure of pure substances. Organic and inorganic compounds. *Industrial and Engineering Chemistry, 39*(4), 517–540.

Sundahl, M., Berg, E., & Svensson, M. (2017). Aerodynamic particle size distribution and dynamic properties in aerosols from electronic cigarettes. *Journal of Aerosol Science, 103*, 141–150.

Tu, H., & Ray, A. K. (2005). Measurement of activity coefficients from unsteady state evaporation and growth of microdroplets. *Chemical Engineering Communications, 192*(4), 474–498.

Turns, S. R. (1996). *Introduction to combustion* (Vol. 287). New York, NY, USA: McGraw-Hill Companies.

Yang, Y. T. (2018). FDA's regulatory shift on tobacco control. *Preventive Medicine, 113*, 153–155.

Zhang, Z., Kim, C. S., & Kleinstreuer, C. (2006). Water vapor transport and its effects on the deposition of hygroscopic droplets in a human upper airway model. *Aerosol Science and Technology, 40*(1), 1–16.

Zhang, Z., Kleinstreuer, C., & Hyun, S. (2012). Size-change and deposition of conventional and composite cigarette smoke particles during inhalation in a subject-specific airway model. *Journal of Aerosol Science, 46*, 34–52.

Zhao, J., Feng, Y., Koshiyama, K., & Wu, H. (2021). Prediction of airway deformation effect on pulmonary air-particle dynamics: A numerical study. *Physics of Fluids, 33*(10), Article 101906.